ACS Catalysis

pubs.acs.org/acscatalysis
Research Article

Understanding the Influence of Iridium Oxide Catalyst State on the Performance in Oxygen Evolution Reaction

Gözde Kardeş, Philipp Röse,* Leonie Wildersinn, Fabian Jeschull, Svetlana Korneychuk, Astrid Pundt, Jan-Dierk Grunwaldt, and Ulrike Krewer*

Cite This: https://doi.org/10.1021/acscatal.5c03350
Read Online

ABSTRACT: Proton-exchange membrane (PEM) water electrolysis is a critical technology for hydrogen production. The oxygen evolution reaction (OER) kinetics at the anode significantly determines the electrolysis performance, requiring the development of active and stable catalysts for high conversion rates. Despite extensive experimental studies, it is still difficult to fully understand how the catalyst state, i.e., the structure, morphology, and oxidation state, which vary by synthesis conditions, affect the OER kinetics and free energies. In this study, we delve into the influence of catalyst calcination on the catalyst state and its relationship with the OER kinetics by a combination of experimental analysis and microkinetic modeling. Our results show that the increasing degree of crystallinity upon calcination and, thus, the reduced number of active sites are the main reason for the decreasing performance of Ir-oxide nanoparticles. Additionally, the water adsorption step becomes thermodynamically more favorable, CUS-mediated PCET and O_2 release are modestly hindered, and the bridge-site redox contribution declines with increasing crystallinity. These subtle, systematic shifts help explain the nonlinear structure−activity relationships reported in the literature. This understanding of the interplay between catalyst synthesis conditions and the OER performance facilitates the tailored design and optimization of high-performance catalysts for more efficient electrocatalytic water electrolysis.

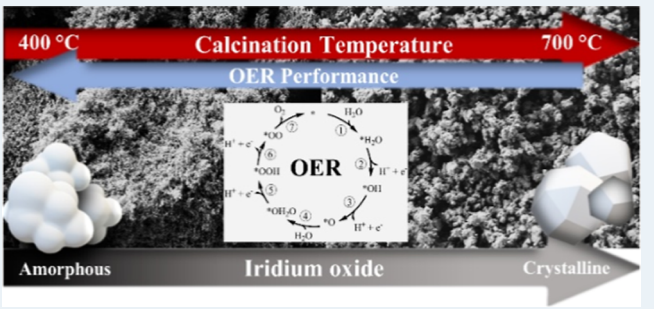

KEYWORDS: *water electrolysis, catalyst characterization, calcination, microkinetic modeling, reaction kinetics, active site density*

1. INTRODUCTION

Proton-exchange membrane water electrolysis (PEMWE) is an attractive technology for the electrocatalytic production of green hydrogen with high conversion rates, enabling efficient energy storage from renewable sources and ensuring energy availability despite seasonal fluctuations.[1,2] However, it suffers from the high anode overpotentials required to achieve technically relevant conversion rates. This primary challenge arises from the slow kinetics of the anodic oxygen evolution reaction (OER), necessitating highly active catalyst materials such as Ir- and Ru-oxides to enhance the electrocatalytic performance.[3] In addition, catalyst stability is vital to ensure prolonged operation under demanding conditions where an acidic environment and high overpotentials accelerate catalyst degradation, ultimately leading to performance reduction.[4,5] The activity and stability of nanoparticulated iridium oxides was analyzed in multiple works.[6−8] Cherevko et al.[9] studied the activity and stability of Ir- and Ru-based catalysts and found that the OER activity is higher for metallic Ir and Ru catalysts than Ir- and Ru-oxides independent of the electrolyte. Their stability, however, shows the opposite trend, making the Ir- and Ru-oxides more stable compared with the metallic Ir and Ru. Geppert et al.[10] revealed in their model-based analysis of iridium oxides that the degradation state of the catalyst influences the OER kinetics, although iridium oxides are notably stable. In another work, Escalera-López et al.[11] showed that increasing the Ir content enhanced the stability of Ir−Ru mixtures, explaining the superior performance of Ir-containing oxides for long-term operation. Optimization of the activity and stability of Ir-based catalysts is thus a crucial focus for industry and researchers.

The extensive research on catalyst design and optimization revealed numerous factors affecting the catalyst activity and stability, e.g., structure,[5,8,12] morphology,[6,13] and oxidation state.[11,14] Moreover, these factors are heavily influenced by catalyst synthesis conditions, such as precursor materials, synthesis methods, and thermal treatment processes following catalyst synthesis. Thermal treatment techniques, particularly calcination, are widely employed in catalyst preparation to

Received: May 16, 2025
Revised: November 21, 2025
Accepted: December 4, 2025

https://doi.org/10.1021/acscatal.5c03350
ACS Catal. XXXX, XXX, XXX−XXX

improve catalyst activity and stability by realizing structural modifications.[15] Several studies have reported the influence of calcination temperature on the catalyst properties such as crystallinity (proportion of catalyst material that is in a crystalline structure compared to an amorphous structure), crystallite size, particle size, oxidation state, and the electrochemically active surface area, ultimately affecting the electrocatalytic performance and stability.[16−18] To date, different research groups have examined the influence of these structural and morphological properties on catalyst performance during oxygen evolution in PEMWE. Reier et al.[19] showed that increasing the calcination temperature increases the crystallite size and, thus, reduces the active surface area and decreases the OER activity. However, they noted that the observed differences in the OER performance are also partly due to the intrinsic nature of the catalyst depending on the applied calcination temperature and not only the change in particle size. Abbott et al.[14] investigated the relationship between the structure and OER activity of nanocrystalline Ir-oxides synthesized by a modified Adams method, followed by calcination at different temperatures, and they observed lower surface areas and higher pore sizes at higher calcination temperatures. However, they detected anomalies in the catalyst's intrinsic activity, which cannot be explained solely by the particle size but also by the exposure of different crystal facets. The study from Danilovic et al.[7] presented how the relationships between the nature of the metal center (i.e., Ir or Ru), morphology, and oxidation state affect the stability and reactivity of monometallic oxides during OER. They found that the catalyst's surface structure and morphology influence the metal atom's valence state and the onset potential of this transition, controlling the density of defect sites. It was also noted that correlating the reactivity as a function of the oxygen binding energy based on ideal catalyst surfaces is impossible. Geiger et al.[6] presented in their study that reduction in active site density due to calcination-induced crystallization, H^+ insertion, and mass transfer limitations due to insufficient water transport are the main reasons of hindered OER activity. Elmaalouf et al.[20] investigated the origin of the electrochemical activity of amorphous iridium oxides, by using a method to separate the influence of oxidation and crystallization occurring due to calcination processes on the catalyst. They concluded that the initial oxidation state has less impact on the catalyst activity than calcination-induced structural changes, i.e., crystallinity and surface area. All in all, the literature observes and agrees with a general correlation among catalyst structure, morphology, and OER activity. However, it remains unclear how these properties influence the free energies and sluggish kinetics of the OER that dictate overall cell performance. Analyzing and quantifying the OER kinetics and free energies solely through experimental work is challenging, leaving a critical gap in understanding the relationship between catalyst state and the OER kinetics. Thus, model-based studies are further required.

In this work, we conduct a comprehensive model-assisted analysis of Ir-oxide nanoparticles, synthesized via flame spray pyrolysis (FSP) and calcined at various temperatures, to elucidate the impact of the catalyst state, specifically structure, morphology, and oxidation state, on oxygen evolution in PEMWE. Although Ir-based oxides, especially disordered or hydrous Ir-oxides, may undergo structural and compositional changes under OER conditions, our approach focuses on how the pristine catalyst state affects the oxygen evolution in PEMWE. In this sense, *ex situ* characterizations are used to provide information into systematic trends in catalyst state as a function of calcination temperature, whereas the dynamic microkinetic modeling focuses on extracting the maximum information from cyclovoltammetry, i.e., from *in situ* electrochemical responses. The model provides insights into the changes in the reaction kinetics, surface coverage of adsorbed species, and reaction energies during dynamic operation as well as the active site density and double-layer capacitance, the structural parameters associated with the catalyst surface that affect the OER performance. To fully describe the observed redox processes, we extend our microkinetic model to account for two surface sites on IrO_x explicitly: the coordinatively unsaturated sites (CUS, often referred to as μ_1 sites) that facilitate the catalytic OER pathway and bridge sites (BRI, associated with μ_2−O/μ_2−OH motifs) that undergo a one-electron surface redox transition. While theoretical and experimental studies indicate that bridge sites are thermodynamically unfavorable for O_2 formation, they can contribute to the current response and thus alter the shape of the pre-OER features in cyclic voltammograms.[21−24]

By linking the catalyst state revealed by *ex situ* measurements with intricate surface processes resolved by dynamic microkinetic modeling, we identify the performance barriers and the underlying processes specific to the catalyst preparation conditions. Overall, our work enables the knowledge-based development of catalyst design strategies to optimize surface structure and properties, ultimately advancing the PEMWE.

2. METHODS

2.1. Catalyst Preparation. In this work, we used as-prepared and post-calcined iridium oxide nanoparticles. As-prepared nanoparticles were synthesized by flame spray pyrolysis (FSP), as reported in detail by Escalera-López et al. and Czioska et al.[11,15] Following the synthesis, the as-prepared Ir-oxide nanoparticles were calcined at 400 °C, 500 °C, 600 °C, and 700 °C. For this purpose, the samples were placed into aluminum oxide crucibles with a cover to avoid the electrostatic movement of the nanoparticles. The samples were calcined in a furnace to targeted temperatures of 400 °C, 500 °C, 600 °C, and 700 °C with a heating rate of 2 °C min^{-1} under air. The samples were kept at maximum temperature for 2 h to ensure homogeneous calcination and then were left in the oven for natural cooling.

2.2. Physical Characterization. The post-calcined iridium oxide samples were characterized in powder form by X-ray diffraction (XRD), X-ray photoelectron spectroscopy (XPS), transmission electron microscopy (TEM), and scanning electron microscopy (SEM) to determine the physical properties of the Ir-oxide nanoparticles, i.e., crystal structure, crystallinity, morphology, and oxidation state.

The XRD measurements were performed using Bruker D8 Advance X-ray Diffractometer with Cu Kα radiation (λ = 1.54 Å) at 40 kV and 35 mA over the 2θ-range of 20−90° with a step size of 0.01°. The XPS measurements were performed using a Kα spectrometer (Thermo Fisher Scientific, East Grinstead, UK), applying a micro-focused, monochromatized Al Kα X-ray source (hν = 1486.6 eV) with 300 μm spot size. In the case of localized surface charging, the binding energy shifts were minimized using the Kα charge compensation system during analysis, using an electron flood gun with low energy-electrons of 8 eV kinetic energy. Spectra in the regions of interest were recorded with a 0.1 eV step, a constant 50 eV

https://doi.org/10.1021/acscatal.5c03350
ACS Catal. XXXX, XXX, XXX−XXX

pass energy, and short-time iteration to monitor any possible sample degradation. Reproducibility was confirmed through three measurements on three different spots on each sample. Further details can be found in SI Section 4. The morphology and structure of Ir-oxide nanoparticles down to the atomic level were studied with TEM. The HAADF (high angle annular dark field) scanning transmission electron microscopy (STEM) images were acquired at 300 keV using an aberration-corrected Thermo Fisher Scientific Themis Z transmission electron microscope with a camera length of 360 mm and selected area aperture of 200 μm. Electron diffraction patterns were acquired with a BM-One View Camera from large agglomerations of nanoparticles for each calcination temperature using a camera length of 360 mm at 300 keV. The mean size of the particles was calculated by accounting for the detected particle sizes based on the TEM pictures. The SEM measurements were performed using a Zeiss 1540 XB Scanning Electron Microscope. Details can be found in Supporting Information Section 3.

2.3. Electrochemical Characterization. The post-calcined Ir-oxide samples were electrochemically characterized by cyclic voltammetry (CV) and electrochemical impedance spectroscopy (EIS) measurements at 25 °C and ambient pressure. A rotating disk electrode (RDE) setup from PINE Research Instrumentation Inc. connected to a Gamry Interface 1010E potentiostat/galvanostat was used for all electrochemical characterizations. We used a PEEK shroud with a glassy carbon disc tip (0.1936 cm^{-2} dia.) as the working electrode, a HydroFlex reversible hydrogen electrode (RHE) from Gaskatel GmbH as the reference electrode, a platinum wire as the counter electrode, and a PTFE cell as the reaction vessel. The reference electrode was pre-conditioned in 0.1 M aqueous H_2SO_4 over at least 24 h, and the working electrode was mirror-polished with 0.3 μm and 0.05 μm alumina suspensions, respectively, to remove impurities on the electrode surface.

The catalyst ink, consisting of 2 mg of the calcined Ir-oxide nanoparticles, was prepared as described previously by Geppert et al. and Escalera-López et al.[10,11,25] Following preparation, the ink was rested for 24 h in a glass vial. Before coating the RDE, it was ultrasonicated for 10 min to avoid precipitation of the nanoparticles at the bottom of the container. A 3-step drop-casting procedure was applied to the working electrode to create a uniform thin film on the glassy carbon surface. Therefore, 10 μL of the ink dispersion was dropped on the electrode in three steps, namely, 3−3−4 μL per drop. After each drop, the electrode was dried in an oven for 5 min at 65 °C.

The electrodes were connected with the RDE setup and immersed in a 0.1 M aqueous H_2SO_4 electrolyte solution in the PTFE cell. The rotation rate was set to 2000 rpm throughout the measurements to avoid mass transport influences by minimizing the diffusion layer thickness of the electrode.

The measurements were performed under air with a protocol consisting of three consecutive voltammograms, each with 200, 100, 50, 25, and 200 mV s^{-1} scan rates, respectively. The potential range for the CV measurements was set to 0.05−1.6 V. Before and after the CV measurements, EIS measurements at open circuit potential were conducted at the frequencies from 10^{-1} to 10^5 Hz with an amplitude of 10 mV_{rms} to measure the ohmic resistance of the electrolyte and, subsequently, to make *iR*-correction of the CV measurements.

2.4. Microkinetic Model of the Oxygen Evolution Reaction. In this study, we employed a dynamic microkinetic model to elucidate the reaction kinetics, surface coverage of the adsorbed species, and reaction energies that govern the dynamic operation. The model reproduces cyclic voltammograms based on a seven-step OER mechanism operating exclusively on coordinatively unsaturated sites (CUS, μ_1) and a set of rate equations describing the surface processes and their changes at the catalyst surface.[10] In some recent studies, it was shown that the bridge sites can undergo redox transitions and contribute to capacitive or pseudocapacitive currents, particularly in hydrous or amorphous Ir-oxides.[23,26,27] However, they reported that bridge sites are not directly involved in O−O bond formation and are thermodynamically unfavorable for oxygen evolution as catalytic centers.[21,23,24] Motivated by these findings, we extend the established CUS-based microkinetic model by adding an independent, reversible one-electron surface redox process on bridge sites (BRI, μ_2) without altering the O−O bond formation pathway and retaining the OER mechanism exclusively on the Ir_{CUS} sites. The bridge-sites share only the electrode potential and the total density of electrochemically available active sites with the CUS sites. The influence of nonfaradaic and other pseudocapacitive processes is captured via non-ideal adsorption isotherms and capacitive terms. In this way, the possible contribution of these processes is also represented in the model, and the OER-relevant energies are determined from the peak positions and shapes on the voltammograms, with all current contributing processes being accounted for. This allows the model to simulate and reproduce experimental CVs over the full potential window while describing the catalytic OER mechanism. Also, in line with the principle of parsimony, our model is constructed to remain as simple as possible while capturing the essential physics of oxygen evolution on Ir-oxide catalyst, as emphasized by earlier modeling frameworks.[28,29]

Models on the OER frequently use density functional theory (DFT) to predict energy values for idealized surfaces, which do not account for the complexities of nanoparticulate, multifaceted catalysts in electrolytes. Our model, in contrast, is built upon experimental data and is specifically designed to handle the non-ideal, mixed catalyst states present in CV experiments. To address structural and energetic heterogeneity, we employ the Hill-de Boer adsorption isotherm, which captures a distribution of lateral interactions between surface species and the spread in electronic surface states. This approach enables the model to accurately reflect the inhomogeneous catalytic behavior observed in non-ideal systems. Our group motivated the model and explained its implementation and validation in detail before.[10,25]

The mechanism of the OER is given in Table 1. The mechanism consists of seven consecutive steps that are water adsorption (steps 1 and 4), proton-coupled electron transfer (steps 2, 3, 5, and 6), and oxygen detachment (step 7). The asterisk, *, represents the coordinatively unsaturated site (CUS) of free Ir.[25] The (110) site of rutile IrO_2 is known for its high stability due to having the lowest surface energy among other surfaces[14,23] and is, therefore, used in this work for simulation studies.

In parallel with the OER mechanism on CUS, we include a separate, reversible one-electron redox process on bridge sites (BRI), associated with μ_2−OH/μ_2−O, given in eq 1.[8,22]

$$\mathrm{BRI-OH} \rightleftharpoons \mathrm{BRI-O} + \mathrm{H^+} + \mathrm{e^-} \quad (1)$$

https://doi.org/10.1021/acscatal.5c03350
ACS Catal. XXXX, XXX, XXX−XXX

Table 1. Elementary Steps of the Oxygen Evolution Reaction Mechanism[10,25,30]

step	reaction
1	$* + H_2O \rightleftharpoons *H_2O$
2	$*H_2O \rightleftharpoons *OH + H^+ + e^-$
3	$*OH \rightleftharpoons *O + H^+ + e^-$
4	$*O + H_2O \rightleftharpoons *OH_2O$
5	$*OH_2O \rightleftharpoons *OOH + H^+ + e^-$
6	$*OOH \rightleftharpoons *OO + H^+ + e^-$
7	$*OO \rightarrow * + O_2$

The CUS and BRI sites do not exchange intermediates and have their own independent coverages. They share only the applied potential, E, and the total electrochemically available active site density, ρ. The bridge fraction, $f_{BRI,}$ denotes the share of BRI sites within ρ and is identified from the experimental CVs. The active site density of CUS sites, ρ_{CUS}, and of BRI sites ρ_{BRI} are then calculated as follows:

$$\rho_{BRI} = f_{BRI}\cdot\rho,\ \rho_{CUS} = (1 - f_{BRI})\cdot\rho,\ f_{BRI} \in [0, 1] \tag{2}$$

The set of equations governing the model comprises the forward/backward reaction rates, $r_{\pm i}$, the adsorption isotherms for forward and backward directions, $f_{\pm i}(\theta)$, the surface coverage balances for adsorbed species, $d\theta_j/dt$, the current density, $j(t)$, and the input function defined as the dynamic electrode potential, $E(t)$.

$$r_{\pm i} = [\prod_{j\in\Omega_{el}} (a_j^{\nu_{\pm ij}})][\prod_{j\in\Omega_{sur}} (\theta_j^{\nu_{\pm ij}})]\cdot f_{\pm i}(\theta)\cdot k_0 \exp\left(\frac{-\Delta G_{a,i} \mp \beta\Delta G_{r,i} \pm \beta|\nu_{ie^-}|eE}{k_B T}\right) \tag{3}$$

Equation 3 describes the reaction rate for each elementary step of the OER on CUS. The equation is derived based on the transition-state theory and Butler−Volmer kinetics. The activity of the electrolyte species is denoted by a_j for $j \in \Omega_{el} = \{H^+; H_2O; O_2\}$. The surface coverage of adsorbed species and the free sites is denoted by θ_j for $j \in \Omega_{sur} = \{*; *H_2O; *OH; *O; *OH_2O; *OOH; *OO\}$. $\Delta G_{r,i}$ represents the difference in the binding energies of the reactant and product species in the forward direction of the elementary steps. The activation free energy, $\Delta G_{a,i}$, represents the energy barrier in the reaction coordinate in both directions. Further values are the stoichiometric coefficient, ν_i of all species Ω and transferred electrons e^-, elementary charge, e, the Boltzmann constant, k_B, temperature, T, the symmetry factor, β, and the preexponential frequency factor, k_0.

$$f_{\pm i}(\theta) = \exp\left(\beta\left[\prod_j \left(\frac{\Delta G_{int,j}}{k_B T}\theta_j\right)^{\nu_{\pm ij}} - \prod_j \left(\frac{\Delta G_{int,j}}{k_B T}\theta_j\right)^{\nu_{\mp ij}} + \prod_j \frac{\theta_j^{\nu_{\pm ij}}}{\theta_j^{\nu_{\mp ij}}} - \prod_j \frac{\theta_j^{\nu_{\mp ij}}}{\theta_j^{\nu_{\pm ij}}}\right]\right),\ \forall\, j \in \Omega_{sur},\ \forall\, i \tag{4}$$

Equation 4 describes the Hill-de Boer adsorption isotherm for each elementary step of the OER on CUS. By this term, the effect of changes in the surface energy state due to areal spacing of the surface sites and the lateral interaction energy of the adsorbed species, $\Delta G_{int,j}$, is considered in the model. The bridge-site redox process follows the same rate expression as eq 3, but with the species defined as $\Omega_{BRI} = \{BRI{-}OH; BRI{-}O\}$ with $\theta_{BRI-OH} + \theta_{BRI-O} = 1$. The BRI redox process has its own thermodynamic and kinetic parameters, i.e., $\Delta G_{r,BRI}$ and $\Delta G_{a,BRI}$. The lateral interactions on the bridge site are also represented in the model with a Frumkin term, $f_{BRI\pm}(\theta_{BRI-OH})$ that depends only on the bridge site coverage (eq 5):

$$f_{BRI\pm}(\theta_{BRI-OH}) = \exp\left(\pm\beta\frac{\Delta G_{int,BRI}}{k_B T}(\theta_{BRI-OH} - 0.5)\right) \tag{5}$$

where θ_{BRI-OH} is the surface fraction of hydroxylated bridge sites, and $\Delta G_{int,BRI}$ is a single interaction parameter for the redox step on BRI. The BRI interaction is formulated to be symmetric around half-coverage, which is appropriate for a two-state redox couple.[31,32]

$$\frac{d\theta_j}{dt} = \sum_i \nu_{ij}\cdot(r_{+i} - r_{-i}),\ \forall\, j \in \Omega_{sur} \tag{6}$$

Equation 6 describes the surface coverage balance of the adsorbed species, $d\theta_j/dt$, during the OER on CUS. It contains the changes due to reaction and sorption processes. On BRI, a single state variable, θ_{BRI-OH}, suffices and its evolution follows the one-electron redox step with the $r_{BRI\pm}$, the BRI-specific free energies, the Frumkin term, and $n = 1$ electron:

$$\frac{d\theta_{BRI-OH}}{dt} = -r_{BRI+} + r_{BRI-} \tag{7}$$

The current density leaving or entering the anode over time, $j(t)$, is the sum of capacitive and faradaic contributions as given in eq 8, and $j_{CUS}(t)$, $j_{BRI}(t)$, and $j_{dl}(t)$ are shown in eqs 8a−c, respectively.

$$j(t) = j_{CUS}(t) + j_{BRI}(t) + j_{dl}(t) \tag{8}$$

$$j_{CUS}(t) = F\cdot\rho_{CUS}\sum \nu_{ie^-}(r_{+i} - r_{-i}) \tag{8a}$$

$$j_{BRI}(t) = F\cdot\rho_{BRI}(r_{+i} - r_{-i}) \tag{8b}$$

$$j_{dl}(t) = C_{dl}\frac{dE}{dt} \tag{8c}$$

Further values are the scan rate, dE/dt, which leads to charge accumulation in the double layer region with the corresponding double-layer capacitance, C_{dl}. In this model, the double-layer capacitance, C_{dl}, is represented as a constant. Such a simplification is necessary, particularly for amorphous or hydrous Ir-oxides, where the measured capacitance may include both electrostatic and pseudocapacitive contributions and because no straightforward experimental method exists to decouple these effects reliably. The constant C_{dl} approximation thus provides a practical means to account for the capacitive background while maintaining the tractability of the model.

$$E(t) = E_0 + t\frac{dE}{dt} - j(t)AR \tag{9}$$

Equation 9 describes the electrode potential, $E(t)$, as the input function for the model. The other parameters are the starting potential, E_0, electrolyte resistance, R, and geometric electrode area, A.

The model parameters are identified based on the mechanism and literature, CV and EIS measurements, and MATLAB global and local search algorithms. The stoichio-

https://doi.org/10.1021/acscatal.5c03350
ACS Catal. XXXX, XXX, XXX−XXX

metric coefficients for species and reactions are determined based on the mechanism. All parameters are given in Supporting Information Sections 6 and 7.

Root mean square error (rmse) is the quality measure for fitting the simulations to the experimental CV curves. Equation 10 describes the rmse calculation, taking the simulated current density, j_{sim}, and the experimental current density, j_{exp}, into account, with $N = 1000$ being the total number of j_{sim} and j_{exp} values at $E > 0.4$ V for the corresponding fitting cycle.[30]

$$\text{rmse} = \sqrt{\frac{1}{N}\sum (j_{sim} - j_{exp})^2} \quad (10)$$

3. RESULTS AND DISCUSSION

3.1. Influence of Calcination on the Catalyst State of Ir-Oxides. The influence of calcination and the resulting catalyst state, i.e., structure, morphology, and oxidation state, on the intricate thermodynamics and kinetics of the underlying reaction processes remains a research topic that defies experimental quantitative investigation. Calcination during catalyst preparation can significantly alter the structure and morphology of the material. Additionally, depending on the pristine state of the as-prepared catalyst material, oxidation of the catalyst particles may occur due to calcination, affecting the OER performance. To investigate the influence of the structure, oxidation state, and morphology of the catalyst on oxygen evolution kinetics and thermodynamics, we used different Ir-oxide samples synthesized and calcined as described in Section 2.1. After calcination, we conducted XRD, TEM, and XPS measurements on each sample. Additionally, we measured the as-prepared iridium oxide sample with XRD and XPS to show the crystallographic structure and oxidation state of the as-prepared sample and how they are affected by the calcination procedure.

Figure 1a shows the XRD patterns of the as-prepared and post-calcined Ir-oxide nanoparticles. The diffractogram of the as-prepared Ir-oxide nanoparticles shows broadened reflections, signifying an amorphous-like structure with minimal ordered crystalline regions for IrO_2, as reported previously by Escalera-López et al.[11] Following calcination, all samples exhibit reflections at $2\theta \approx 28°$ (110), 34.8° (101), 54° (211), 69.3° (301), 73.2° (202), and 83.1° (321), characteristic of tetragonal rutile-type IrO_2 and in good agreement with the database shown in Figure 1b. The observed slight shifts from the exact 2θ positions might be attributed to the beam divergence of the XRD due to sample placement.[33] Starting from 400 °C, the reflections of (110), (101), (211), (301), and (321) become more prominent and sharper as the calcination temperature rises to 700 °C. The (200) reflection significantly decreases in intensity and shifts slightly toward lower angles at 600 and 700 °C, possibly by expansion of the unit cell. Increasing sharpness indicates larger crystallites and particles. Additionally, the intensities of the (101) and (110) reflections increase with increasing calcination temperature, with (110) rising the most, indicating predominant crystallization of the (110) plane. The (110) plane of rutile IrO_2 and its impact on OER performance and stability has been a topic of interest for many research groups. Over investigated the structure–property relationships of IrO_2 and RuO_2 and stated that the OER activity of IrO_2 and RuO_2 is structure sensitive.[24] Kwon et al. showed that (100), (001), and (110) planes of IrO_2 have higher activity during the OER compared to others.[34] Pfeifer et al. demonstrated that amorphous iridium oxides are more active than crystalline ones during the OER.[35] Stoerzinger et al. observed that the OER activity of IrO_2 and RuO_2 increases during potential cycling, partially due to the formation of an amorphous layer on the surface of the facet.[36] Given the XRD results and literature, a substantial decrease in electrocatalytic activity may occur, especially at higher calcination temperatures, due to the predominant crystallization of the (110) plane. On the other hand, the diffractograms display no indication of metallic iridium (face-centered cubic, fcc), which is supposed to exhibit all the reflections shown in Figure 1b. Thus, it can be concluded that the amorphous regions of tetragonal rutile IrO_2 in the as-prepared sample are subjected to crystallization, which may affect the performance by reducing the number of available active sites. Nevertheless, it should be mentioned that the catalyst performance may also be influenced by morphological differences between the catalyst samples, which we investigate with TEM measurements in the following.

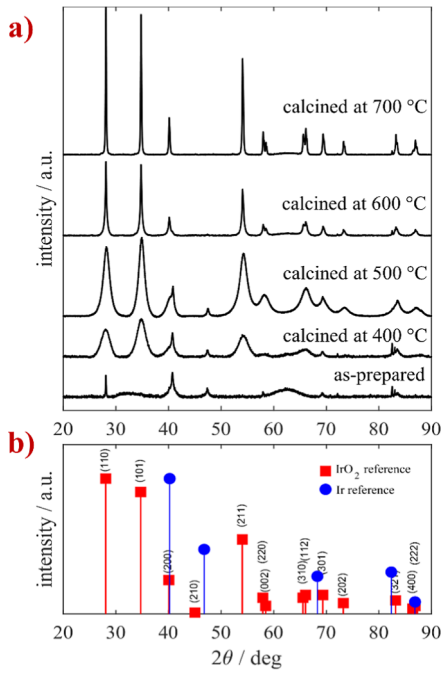

Figure 1. X-ray diffractograms for (a) as-prepared and post-calcined (at 400 °C, 500 °C, 600 °C, and 700 °C) Ir-oxide nanoparticles, and (b) the reference spectrum for the tetragonal rutile IrO_2 (JPCD card no. 15-0870), and Ir fcc (COD, 1512514). The diffractograms were smoothened and the reflections were numbered only for the IrO_2 reference. Individual XRD diffractograms for each sample are shown in Figure S1.

Figure 2 shows the STEM images for the post-calcined Ir-oxide samples, demonstrating the morphology change of the nanoparticles depending on the calcination temperature. The size of the nanoparticles calcined at 400 °C ranges from 3 to 7 nm. When the calcination temperature is increased to 500 °C, the nanoparticles grow, reaching 6–9 nm. The sample calcined at 600 °C contains small particles ranging from 12 to 19 nm, and large particles ranging from 100 to 200 nm. The size of the particles calcined at 700 °C appeared to be 20–39 nm. This is in agreement with the sharp reflections in the XRD patterns observed for the samples calcined at 600 and 700 °C. The mean particle size calculated based on the TEM results is 4, 7.5, 15, and 30 nm for the Ir-oxide nanoparticles calcined at

https://doi.org/10.1021/acscatal.5c03350
ACS Catal. XXXX, XXX, XXX–XXX

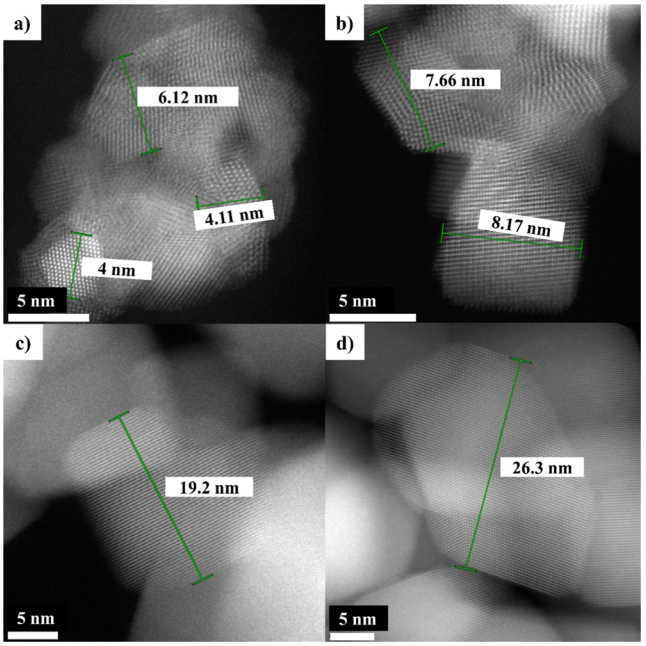

Figure 2. TEM images of the Ir-oxide nanoparticles calcined at (a) 400 °C, (b) 500 °C, (c) 600 °C, and (d) 700 °C.

400 °C, 500 °C, 600 °C, and 700 °C, respectively. Additionally, the total surface area of the nanoparticles coated on the RDE surface is estimated based on the electrode surface area, catalyst loading, and mean particle size of the samples based on their TEM images. Here we note that spherical, non-aggregated particles are assumed for estimation of the total surface area, and this allowed for relative comparison across identically prepared electrodes. Given that all electrodes had an identical geometric area and Ir loading, this approach provides a consistent basis on which to compare the intrinsic activity of samples with different crystallite sizes. The total surface area of nanoparticles decreased by 45.3% from the Ir-oxide sample calcined at 400 to 500 °C, by 50.3% from 500 to 600 °C, and by 48.6% from 600 to 700 °C with respect to the state before. It is evident that the size of the nanoparticles dramatically increases and the surface area decreases when the calcination temperature rises from 400 to 700 °C. Besides, crystalline structures are observed at every calcination temperature. However, the electron diffraction data (see Figure S2) shows that the ring diffraction pattern obtained for the samples calcined at 400 °C is broader than that of the other samples, suggesting that the nanoparticles calcined at 400 °C are not fully crystallized and include some amorphous structures. Overall, the TEM results show increasing particle size with increasing calcination temperature and agree with the XRD analysis, indicating a higher crystallinity at higher calcination temperatures.

Figure 3a and b show the XPS results obtained for Ir-oxide powder samples that are as-prepared and calcined at 400 and 700 °C to identify further notable trends caused by increasing calcination temperature. A detailed overview of all high-resolution spectra for O 1s, C 1s, and a full scan survey for the other Ir-oxide samples are displayed in Figures S4 and S5. All spectra were referenced to the hydrocarbon C 1s peak (C−C and C−H) at 284.6 eV (Figure S4b). Corresponding details of binding energies (eV) and atomic percentages (atomic-%) of the XPS quantification are reported in Tables 2 and S1. The survey scans (Figure S5) show the presence of iridium, oxygen, and a small fraction of carbon, suggesting that there are no impurities of other elements before and after the calcination. Figure 3a shows the asymmetric line shape in the 4f region, which was observed for all samples, where the asymmetry increases at higher calcination temperatures. This asymmetry is characteristic of rutile-type IrO_2, which is defined by two

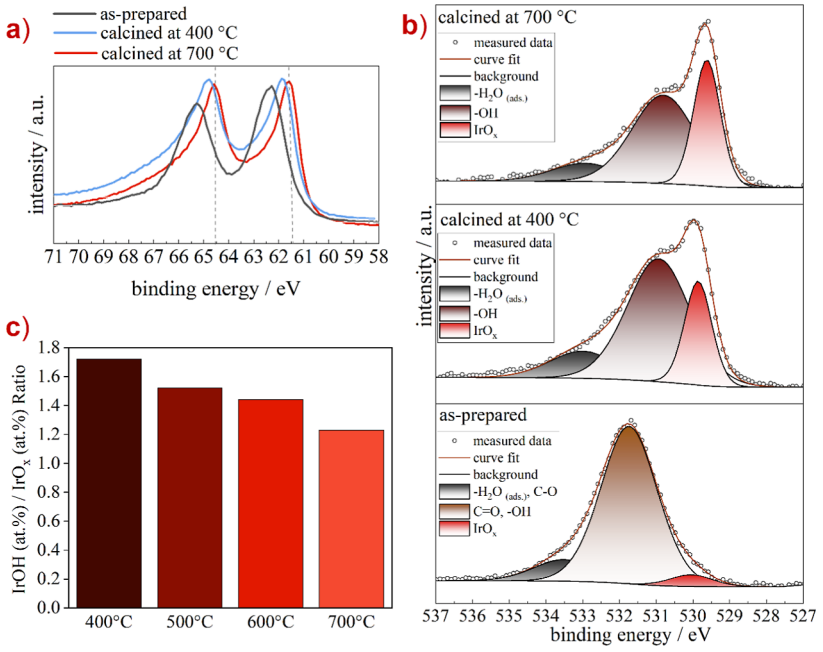

Figure 3. XPS analyses on as-prepared and post-calcined Ir-oxide nanoparticles: (a) high-resolution Ir 4f spectra for the as-prepared Ir-oxide sample as well as the samples calcined at 400 and 700 °C, (b) high-resolution O 1s spectra of the Ir-oxide nanoparticles as-prepared (bottom, gray line), calcined at 400 °C (middle, brown line), and calcined at 700 °C (top, red line), and (c) hydroxide-to-oxide ratio for the post-calcined Ir-oxide nanoparticles.

https://doi.org/10.1021/acscatal.5c03350
ACS Catal. XXXX, XXX, XXX−XXX

Table 2. Summary of the XPS Fits for the Ir-Oxide Nanoparticles: As-Prepared and Calcined at 400 and 700 °C[a]

sample/peak	binding energy/eV	atomic-%	fwhm/eV
	Ir-oxide as-prepared		
Ir−O	530.0	2.3	1.3
Ir−OH, C═O	531.7	42.0	1.8
H_2O, C−O	533.5	6.0	1.9
	Ir-oxide calcined at 400 °C		
Ir−O	529.9	16.9	1.0
Ir−OH	530.9	29.0	1.7
H_2O	533.0	2.0	1.9
	Ir-oxide calcined at 700 °C		
Ir−O	529.7	19.6	1.0
Ir−OH	530.8	24.1	1.7
H_2O	533.0	1.8	1.9

[a]The table shows the binding energy, atomic concentration, and fwhm (full-width-at-half-maximum) for the corresponding peak positions.

primary features: the peaks of Ir $4f_{7/2}$ and Ir $4f_{5/2}$. In the case of Ir-oxide calcined at 700 °C, these peaks are located approximately at 61.7 and 64.7 eV, closely mirroring previously documented values[12,37] and can be attributed to the rutile-type Ir(IV). For the Ir-oxide nanoparticles calcined at 400 °C, there is a slight shift toward higher binding energies for the Ir 4f peaks. Here, the main peaks for Ir $4f_{7/2}$ and $4f_{5/2}$ are observed at around 61.9 and 64.8 eV, respectively. In comparison, the as-prepared Ir-oxide sample is noticeably shifted to higher binding energies with peaks for Ir $4f_{7/2}$ and $4f_{5/2}$ at 62.3 and 65.3 eV. This shift reflects deviations from the rutile IrO_2 coordination environment. Recent literature attributes such shifts to the presence of undercoordinated Ir species (e.g., Ir(III)) in disordered or short-range-ordered oxides, where the local atomic arrangement differs from the fully crystalline rutile structure.[12,38] For instance, amorphous or poorly crystallized Ir-oxides often show higher Ir 4f binding energies due to reduced Ir−O coordination and the stabilization of mixed Ir^{3+}/Ir^{4+} states.[39] These states are frequently associated with surface hydroxides or oxygen vacancies in metastable oxides within the surface and outer subsurface layers, consistent with the coexistence of hydroxide species detected in our XPS O 1s signal (Figure 3b). Therefore, the energy shift was ascribed to the presence of Ir(III) species, as indicated by prominent peaks at 62.3 and 65.3 eV for Ir $4f_{7/2}$ and Ir $4f_{5/2}$, which indicate the mixed state of Ir(III/IV). The limited XPS probing depth (~10 nm) further contextualizes these observations. For the as-prepared and at 400 and 500 °C calcined samples with a mean particle size below 10 nm, XPS interrogates the entire particle volume, amplifying contributions from surface/near-surface species. In such small particles, surface effects dominate: Ir^{3+}-rich suboxides, hydroxylation, or defects (e.g., oxygen vacancies) likely pervade the structure rather than being confined to a thin outer layer. At higher calcination temperatures, i.e., 600 and 700 °C, however, particle growth (>20 nm) restricts XPS analysis to the outermost of the particle volume. While this reduces sensitivity to bulk composition, the retained surface features (e.g., residual hydroxides, reconstructed interfaces) may still influence catalytic behavior. Notably, the non-proportional decline in OER activity with increasing particle size suggests that surface properties—rather than bulk crystallinity—dominate performance, as even larger particles retain catalytically active sites (e.g., metastable suboxides, defect-rich surfaces). The O 1s spectra (Figures 3b and S4a) of the post-calcined samples, i.e., 400 °C, 500 °C, 600 °C, and 700 °C, show three main species identified at around 529.6, 530.8, and 533.0 eV, attributed to Ir−O and Ir−OH bonds, and adsorbed water molecules on the surface, respectively. In the as-prepared sample, an additional contribution appears at ~286.1 eV attributed to C−O species (see Table S1a), shifting the H_2O peak to ~533.5 eV. Furthermore, an O 1s peak at ~531.7 eV is observed in the as-prepared Ir-oxide particles. This feature can be attributed to multiple factors. While storage under ambient conditions and preparation outside the glovebox introduce moisture (contributing to the −OH signal), the presence of residual organic species from the synthesis process must also be considered. The slurry, composed of a mixture of methanol and acetic acid, served as the solvent for the iridium acetylacetonate precursor. During flame spray pyrolysis (FSP), the precursor is expected to decompose; however, incomplete decomposition in the uncalcined sample may leave residual acetylacetonate (acac) ligands. These acac ligands contain carbonyl (C═O) groups, which could contribute to the C═O component of the peak of the O 1s peak. This is consistent with the observed adventitious carbon in the C 1s spectra, which may overlap with carbon from residual acac (Figure S4b). Table 2 displays the binding energy, atomic percentages, and full-width-at-half-maximum (fwhm) values of each Ir-oxide sample. The results show that the percentage of −OH and other contributions from C═O decreases from 42% to 24% when the as-prepared Ir-oxide sample is calcined at 700 °C. Figure 3c shows the calculated hydroxide-to-oxide ratio of the individual calcined samples with a decreasing fraction of the −OH species with increased temperature. The amorphous Ir-oxide powder exhibits complex Ir 4f XPS line shapes due to overlapping contributions from mixed Ir^{3+}/Ir^{4+} states, residual acetylacetonate ligands from incomplete precursor decomposition, and surface hydroxides. For the sample calcined at 700 °C, the Ir 4f XPS spectra (Figure 3a) confirm the coexistence of Ir(IV) and Ir(III) species with Ir(IV) dominating. This is evident from the stronger contribution of the Ir^{4+} component at a binding energy (BE) of ~61.8 eV, consistent with the literature values for rutile IrO_2, compared to the weaker Ir^{3+} signal at ~62.4 eV. The broadening of the Ir 4f peak for the as-prepared particles suggests incomplete conversion to stoichiometric IrO_2, with coexisting surface species likely arising from residual hydrated structures (e.g., $IrO_2{\cdot}(H_2O)_x$). These hydrated phases, mainly formed during particle synthesis and air exposure, persist even after calcination at 400−700 °C, as indicated by the O 1s spectra. While calcination decreases the fraction of hydrated species, the process is insufficient to achieve a pure rutile structure, likely due to limited thermal energy or duration. Notably, no metallic Ir^0 was detected by XPS or XRD, confirming oxides dominate under given calcination conditions. In summary, the XPS analysis reveals that increasing calcination temperature reduces the content of hydroxides and organic residues on the surface, improving the purity of a few outer atomic layers of the catalyst surface and structural order. XPS results further confirm the improved crystallinity at higher calcination temperatures, as shown by XRD. However, some hydrated, defect-rich surface species remain, suggesting incomplete transformation into fully crystalline IrO_2, which could impact the OER performance. It is worth noting that Ir(III) species are not explicitly modeled as catalytic

https://doi.org/10.1021/acscatal.5c03350
ACS Catal. XXXX, XXX, XXX−XXX

intermediates. As suggested by several experimental and theoretical works, Ir(III) species typically act as precatalytic states or redox spectators under OER-relevant conditions, whereas the active turnover predominantly occurs via Ir(IV/V)=O motifs on undercoordinated surface sites. Nevertheless, the presence of Ir(III) may influence the electrochemical environment indirectly by contributing to pseudocapacitance, altering local adsorption or reaction energetics or affecting site accessibility. These effects are partially covered by the model parameters such as active site density (ρ) and adsorption isotherms, which vary systematically with calcination temperature and structural disorder (see Section 2.4).

To better interpret the surface chemistry trends observed via XPS, we compare our findings with a recent study by Roiron et al.,[40] who proposed a structural descriptor model based on O 1s spectral components to classify Ir-oxide surfaces along the amorphous−crystalline spectrum. Although the O 1s spectra were not fitted using structurally resolved bridging oxygen species due to our mechanistic assumptions, a shift from mixed Ir(III)/Ir(IV) states toward Ir(IV)-dominated surfaces, accompanied by a decrease in hydroxyl and defect-related species, is observed with increasing calcination temperature.

3.2. Influence of Calcination on OER Characteristics.

In this section, we analyze the influence of calcination on the OER performance of catalyst nanoparticles using cyclic voltammetry (CV). Figure 4 shows the CV curves of the post-calcined Ir-oxide nanoparticles at 200 mV s^{-1} scan rate. The CV measurements were conducted in 0.1 M H_2SO_4 electrolyte solution at room temperature. All potentials are referred to RHE and are *iR*-corrected. The CVs of each sample recorded at varying scan rates are given in Figure S6 for better visualization and to show the stability of the CVs during measurements. The post-calcined samples exhibit a constant current behavior starting from ~0.20 V (unless otherwise stated, all potentials in this work are given relative to the RHE) due to double-layer charging and discharging. A decrease in double-layer current is observed with increasing calcination temperature, resulting from the decreasing double-layer capacitance, likely due to the reduction of the electrochemically active surface area. The potential window for the double-layer region slightly increases at higher calcination temperatures, with the widest range observed for nanoparticles calcined at 700 °C (~0.2 V−0.50 V), attributed to the increased order-range of the surface at higher temperatures. To further assess the role of capacitive contributions and their evolution with thermal treatment, the CVs were normalized with respect to the scan rate and compared to their original forms (Figures S6 and S7). This comparison shows that pseudocapacitive effects are more pronounced in the lower-temperature samples and become progressively less significant as the calcination temperature increases.

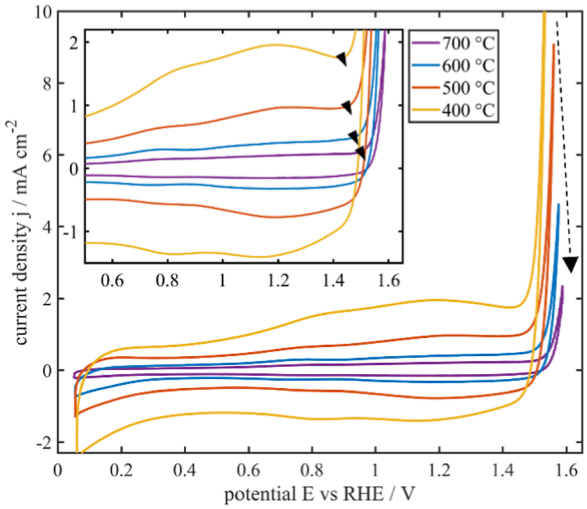

Figure 4. Cyclic voltammograms of the post-calcined Ir-oxide nanoparticles. The inset shows a magnified view of the pre-OER region, with black arrow-shaped markers indicating the approximate potential at which the current begins to increase steeply. These values were determined by calculating the first derivative of the CVs (d*j*/d*E*) and identifying the potential at which the derivative begins to rise continuously, corresponding to the onset of rapid current increase associated with the OER. These points are used for relative comparison only and should not be interpreted as precise onset potentials of the OER.

Between the capacitive region and the potential where the OER current begins to rise sharply, all voltammograms exhibit two distinct redox features in the forward scan (note: the term "OER onset potential" is deliberately avoided as suggested by Batchelor-McAuley[41]). The precise determination of the onset potential of the OER is complicated due to the possible overlap of pseudocapacitive and faradaic currents, particularly for the samples calcined at lower temperatures, where surface hydroxylation and disorder amplify pseudocapacitive contributions. The onset of the first redox feature starts around 0.33 V, 0.39 V, 0.44 V, and 0.51 V for nanoparticles calcined at 400 °C, 500 °C, 600°C, and 700 °C, respectively. The feature in this potential region is mainly associated with the water adsorption onto the catalyst surface ($* + H_2O \rightleftharpoons *H_2O$) coupled with the first PCET step ($*H_2O \rightleftharpoons *OH + H^+ + e^-$), according to the conventional stepwise OER mechanism.[3,23,36,42,43] These results also align with those obtained by Geppert et al.,[10] for the Ir-oxide samples calcined at temperatures above 400 °C. Further on, the same feature shows a peak or inflection point at around 0.85 V, 0.78 V, 0.75 and 0.75 V for the respective samples. Among others, IrO_x calcined at 400 °C shows the broadest feature and highest current density, as the potential window of this specific feature narrows down, and the current density decreases with the increasing calcination temperature. One plausible explanation for the lower current densities is reduction of available active sites by growing crystallite/particle size as discussed in the last section. Additionally, the transition from short-range ordered to long-range ordered crystal structures at higher calcination temperatures may limit the PCET steps to the topmost surface layer, hindering proton penetration into the bulk and preventing subsurface Ir atoms from reacting, as suggested by Mom et al. and Liang et al.[8,22] Conway and Mozota[44] showed in their work that the charge storage and redox activity extend beyond the outer surface in hydrous Ir-oxide films. Similarly, Saveleva et al.[45] demonstrated how the changes in the oxidation state propagate into the subsurface of IrO_x films under OER conditions, especially in amorphous or partially hydrous materials. Binninger et al.,[46] on the other hand, suggested lattice oxygen involvement, especially in disordered structures, based on their DFT calculations. Nevertheless, this behavior may also be attributed to changes in the free reaction energies due to alterations in the catalyst surface caused by calcination, which we investigated via our microkinetic model.

A further peak point is identified at around 1.19 V and 1.23 V for the particles subjected to calcination at 400 and 500 °C,

https://doi.org/10.1021/acscatal.5c03350
ACS Catal. XXXX, XXX, XXX−XXX

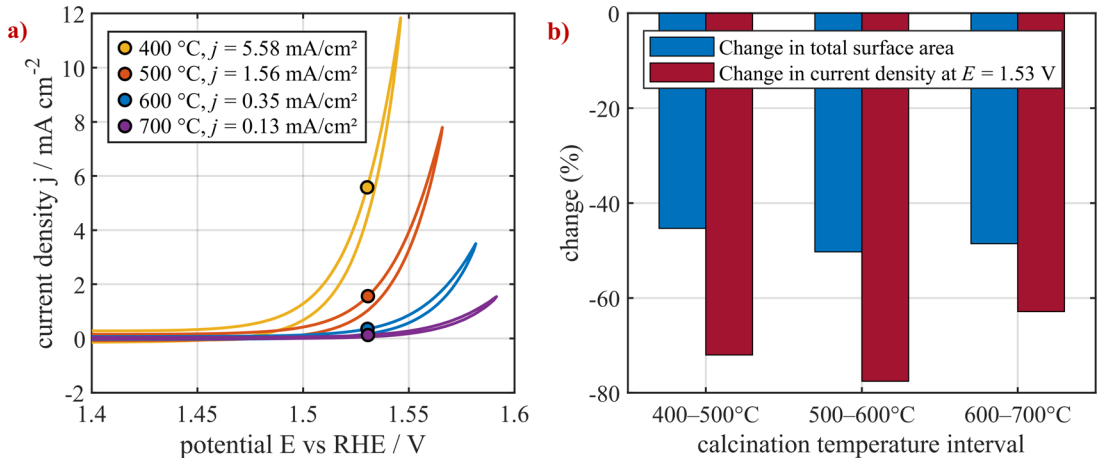

Figure 5. Effect of calcination temperature on catalytic activity and estimated surface area. (a) CVs of the post-calcined samples recorded at a scan rate of 25 mV s^{-1} with the current density at 1.53 V ($j_{@1.53\ V}$) extracted for each sample. (b) Comparison of the changes in $j_{@1.53\ V}$ with the changes in the estimated total surface area.

respectively. This peak evolves into a broad shoulder for samples calcined above 600 °C, making it difficult to determine the exact peak potential. The shoulder starts from the preceding inflection at 0.89 V and continues until 1.38 V for the Ir-oxide nanoparticles calcined at 600 °C. A similar situation is observed for the Ir-oxide nanoparticles calcined at 700 °C, where the shoulder starts at 0.9 V and extends to ∼1.43 V. Both shoulders show a subtle non-linear increase from the given inflection points to their apparent OER onset potentials, indicating a superposition of processes within a similar potential window. It is possible that two distinct peaks representing the second ($*OH \rightleftharpoons *O + H^+ + e^-$) and third PCET steps ($*OH_2O \rightleftharpoons *OOH + H^+ + e^-$) overlap within this potential range. A recent work by Liang et al.[27] attributes the current response in this potential range dominantly to the non-catalytic redox transition on the bridge site ($BRI{-}OH \rightleftharpoons BRI{-}O + H^+ + e^-$) rather than the OER steps. However, it should be noted that depending on catalyst morphology, structure, and measurement conditions (e.g., electrolyte solution, operating temperature), the position and relative contributions of CUS and BRI sites in CVs may differ. To clarify these contributions, our extended microkinetic model explicitly accounts for both the OER processes on CUS and the non-OER redox processes on BRI sites while reproducing the entire CV. The results obtained from the model will be discussed in the following chapters.

The potential where the OER current begins to rise sharply indicates the rapid progression of all species involved in the OER mechanism toward forming molecular oxygen. These potentials are approximately 1.43 V, 1.44 V, 1.46 V, and 1.48 V for nanoparticles calcined at 400 °C, 500 °C, 600 °C, and 700 °C, respectively. According to Binninger et al., the shift of the OER toward higher potentials can be attributed to the changing activation barrier of the fourth PCET step ($*OOH \rightarrow *OO + H^+ + e^-$) and the accompanying oxygen detachment step ($O_2 \rightarrow * + O_2$).[47] Increased activation energies due to surface alteration, thus, may result in hindered kinetics, shifting the pre-OER region to higher potentials. Besides, the more amorphous structure facilitates easier O_2 desorption due to various coordination sites with weaker binding energies, which can explain the lower OER potential of Ir-oxide samples calcined at lower temperatures.

Lastly, the redox peaks, j_{max}, are measured as 13.81 mA cm^{-2} at 1.54 V for 400 °C, 9.08 mA cm^{-2} at 1.56 V for 500 °C, 4.62 mA cm^{-2} at 1.58 V for 600 °C, and 2.34 mA cm^{-2} at 1.59 V for 700 °C at 200 mV s^{-1}. The results represent a clear decrease in j_{max} and also a shift in potential toward higher values as the calcination temperature increases. However, comparing all the samples at a specific potential is more appropriate in order to compare their activity. Figure 5a shows the current densities measured at the specific potential of 1.53 V, $j_{@1.53\ V}$ for each post-calcined sample at the scan rate of 25 mV s^{-1}. The determined values are 5.58 mA cm^{-2} for 400 °C, 1.56 mA cm^{-2} for 500 °C, 0.35 mA cm^{-2} for 600 °C, and 0.13 mA cm^{-2} for 700 °C. These results show a substantial decrease in $j_{@1.53\ V}$, with a reduction of 72.1% when the calcination temperature increases from 400 to 500 °C, a further significant drop of 77.6% from 500 to 600 °C, and another reduction of 62.9% from 600 to 700 °C. This significant decrease with increasing calcination temperature may be attributed to increasing particle size and crystallinity, which reduces the number of active sites. For relative comparison across the identically prepared electrodes, we estimated the total physical surface area of the catalysts based on the TEM-determined mean particle size, assuming spherical and non-aggregated particles. Given that all electrodes have an identical geometric area and Ir loading, this approach provides a consistent basis to assess changes in intrinsic activity with particle size. However, Figure 5b shows that the observed performance loss cannot be fully explained by the particle growth and corresponding decrease in the physical surface area alone, especially at lower calcination temperatures. To further decouple the effects of surface area from intrinsic catalytic behavior, CVs with currents normalized to the estimated total physical surface area of each sample are listed in Figure S9. Even after normalization, the trend of decreasing current density with increasing calcination temperature persists, indicating that additional surface-related processes, affected by structural factors beyond geometric surface area, i.e., crystallinity, surface order, and defect density, contribute to the observed decrease in activity. Therefore, the impact of calcination and resulting crystallinity on OER's intricate thermodynamics and kinetics must be further investigated. As mentioned earlier, understanding these intricate properties is experimentally challenging. Thus, our

https://doi.org/10.1021/acscatal.5c03350
ACS Catal. XXXX, XXX, XXX−XXX

microkinetic model plays a significant role in understanding the catalyst behavior in relation to its state.

3.3. Influence of Calcination on Surface Energetics and Reaction Kinetics during the OER. In this section, we investigate how calcination affects the thermodynamics and kinetics of the oxygen evolution reaction (OER). We thoroughly analyze the impact of the degree of crystallinity of Ir-oxide catalysts on the OER kinetics, which cannot be fully explained by the growing particle size, using a dynamic microkinetic model (see Section 2.4).

Figure 6 shows the comparison between experimental and simulated cyclic voltammograms for Ir-oxide nanoparticles

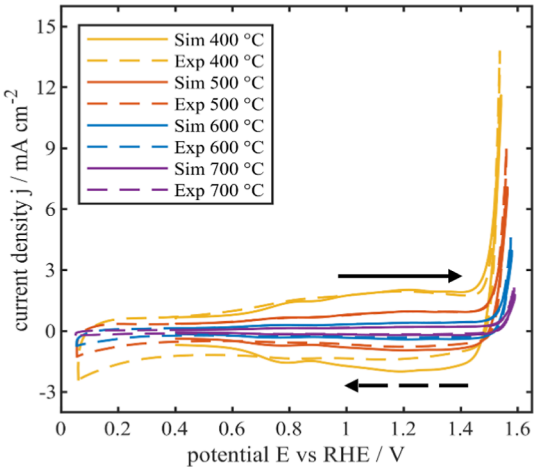

Figure 6. Experimental (dashed lines) and simulated (straight lines) CV curves on the Ir-oxide nanoparticles calcined at 400 °C, 500 °C, 600 °C, and 700 °C. Arrows indicate the sweep direction as forward (solid arrow) and backward (dashed arrow).

calcined at different temperatures (400 °C, 500 °C, 600 °C, and 700 °C) for the scan rate of 200 mV s^{-1}. Additionally, to demonstrate the model's ability to reproduce CVs at varying scan rates, we show a very good match of experimental and simulated CVs at multiple scan rates (25−200 mV s^{-1}) in Figure 7 for all post-calcined Ir-oxide samples. All experiments were conducted in a 0.1 M H_2SO_4 solution at 25 °C. Potentials are referred to RHE and are *iR*-corrected. The simulated voltammograms show commendable agreement with the experimental curves, as indicated by the calculated root-mean-square error (rmse) values of 0.382, 0.148, 0.057, and 0.029 mA cm^{-2} for the iridium oxide samples calcined at 400, 500, 600, and 700 °C, respectively. The forward sweep is in excellent accordance with the experiments, while deviations can be observed in the backward sweep, particularly pronounced for the Ir-oxide nanoparticles calcined at 400 °C. These deviations diminish with increasing calcination temperature and are least visible for the more crystalline samples. This trend can be attributed to the enhanced stability and structural definition of the catalysts, which reduce the extent of redox hysteresis and surface reorganization. The asymmetry observed in the CV of the 400 °C sample likely originates from redox hysteresis due to structural disorder and surface hydration. This sample exhibits higher Ir(III) and −OH content in XPS, as well as broader redox features in CV, which suggests a more flexible and disordered surface. Such surfaces may undergo irreversible or delayed transitions (e.g., site deactivation or relaxation) during the oxidation sweep, which are not fully reversed during reduction. For better visibility, the CV measurements and simulations for each Ir-oxide sample are shown in Figures S10a−13a. Additionally, different scan rates of each CV measurement are simulated along with 200 mV s^{-1}. Figures S10b−S13b show that the experimental scan rate dependence is excellently reproduced by the model.

Figure 8 depicts the double-layer capacitance, the density of active CUS sites, and the current density at the applied potential E = 1.53 V (*iR*-corrected) obtained from the simulations for Ir-oxide samples calcined at different temperatures. Increasing the calcination temperature from 400 to 500 °C causes a decrease of 45.7% in double-layer capacitance, C_{dl}, and a decrease of 53.1% in the density of electrochemically available CUS sites, ρ_{CUS}. The simulated current density at E = 1.53 V, $j_{@1.53\ V,sim}$, also decreases by approximately 66.1%. Similarly, increasing the calcination temperature from 500 to 600 °C significantly decreases C_{dl} by 64.1% and ρ_{CUS} by 43.4%. $j_{@1.53\ V,sim}$ substantially decreases by approximately 65.5% when the calcination temperature is increased from 500 to 600 °C. Lastly, changing the calcination temperature from 600 to 700 °C results in a sharp decrease in C_{dl} by 57.9%, in ρ_{CUS} by 46.1%, and in $j_{@1.53\ V,sim}$ by 56.5%. Parallel to these findings, the estimated apparent capacitance (Figure S8) shows a clear monotonic decrease from ∼4.02 μF cm^{-2} (400 °C) to ∼0.35 μF cm^{-2} (700 °C). This trend further supports the reduction of surface hydroxide coverage and the electrochemically active area at higher temperatures, in line with XPS and microkinetic model results. Together, these results show that the influence of pseudocapacitive processes is most pronounced at low calcination temperatures and becomes more suppressed as the crystallinity and structural order improve.

It can be concluded that the decrease in the density of active CUS sites and double-layer capacitance at higher calcination temperatures strongly correlates with the observed reduction in current density at 1.53 V and can be primarily attributed to particle growth induced by increased calcination temperatures. However, the reduction in $j_{@1.53\ V,sim}$ does not scale linearly with the reductions in ρ_{CUS} and C_{dl}, particularly at lower calcination temperatures. For instance, $j_{@1.53\ V,sim}$ decreases by 66.1% between 400 and 500 °C, while ρ_{CUS} and C_{dl} decrease by approximately 55% and 46%, respectively. Furthermore, the rate of decline in $j_{@1.53\ V,sim}$, ρ_{CUS}, and C_{dl} slows at higher calcination temperatures despite continued particle growth.

To better understand this non-linear relationship between particle size, active site density, and catalytic performance, we examined the changes in surface functionality as captured by XPS. The relative intensity of the Ir−OH component in the O 1s spectrum, representing hydroxylated, undercoordinated surface oxygen, decreases from ∼42% in the as-prepared sample to ∼24% when calcined at 700 °C (Table 2), consistent with a loss of reactive surface species. This trend also closely mirrors the reduction in the density of active CUS sites (ρ_{CUS}) from 26.3 × 10^{-9} mol cm^{-2} to 3.09 × 10^{-9} mol cm^{-2} across the same temperature range. While XPS captures the total presence of Ir−OH species, the model-derived ρ reflects only kinetically accessible sites under the OER conditions. The steeper decline in ρ may therefore indicate that a fraction of the remaining Ir−OH species becomes inactive due to reduced conductivity, reduced proton accessibility, or unfavorable binding energies.

These findings indicate that while the reduction in active site density strongly impacts the OER activity, additional surface

https://doi.org/10.1021/acscatal.5c03350
ACS Catal. XXXX, XXX, XXX−XXX

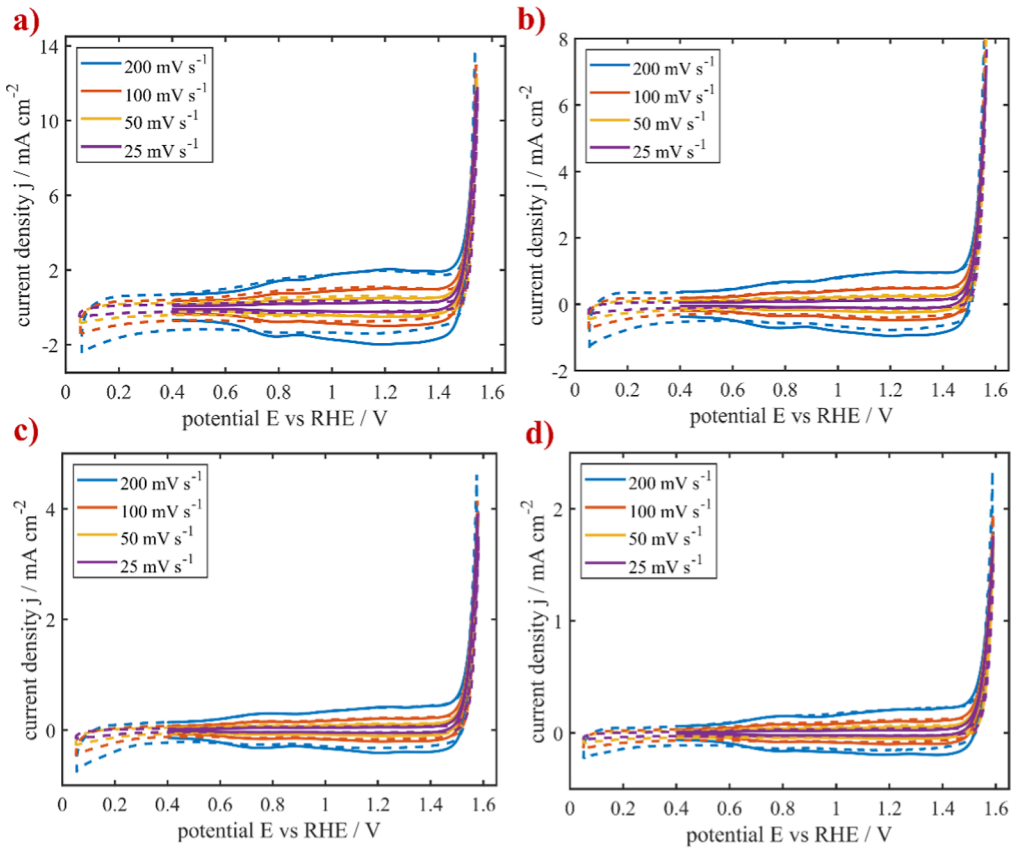

Figure 7. Experimental (dashed lines) and simulated (straight lines) CV curves recorded at the scan rates of 200, 100, 50, and 25 mV s^{-1} for the Ir-oxide nanoparticles calcined at (a) 400 °C, (b) 500 °C, (c) 600 °C, and (d) 700 °C.

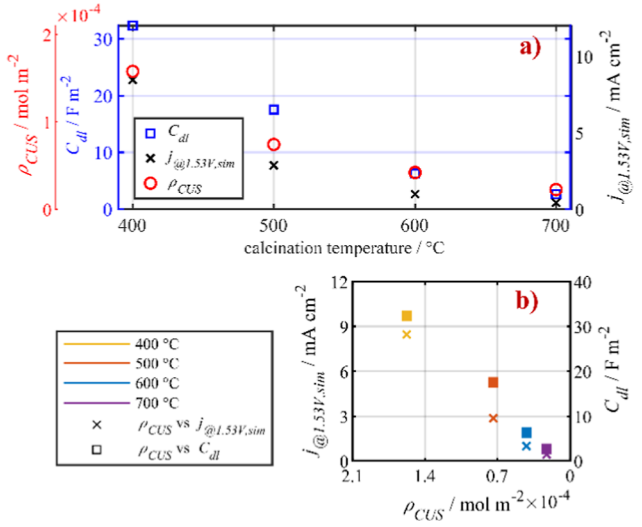

Figure 8. Evaluation of parameters extracted from the simulations for the postcalcination Ir-oxide nanoparticles: (a) simulated current density at E = 1.53 V, $j_{@1.53\ V,sim}$, double layer capacitance, C_{dl}, and density of available active CUS sites, ρ_{CUS}, versus calcination temperature, (b) double-layer capacitance, C_{dl}, and the simulated current density at E = 1.53 V, $j_{@1.53\ V,sim}$, versus density of active CUS sites, ρ_{CUS}.

processes influenced by varying crystallinity induced by calcination temperature may also affect the OER performance. To find out the possible changes in the processes on the catalyst surface that resulted in a non-linear relationship between active site density, particle size, and performance, we investigated the energy differences among post-calcined catalysts, as depicted in Figure 9. All of the results obtained from the microkinetic model ($\Delta G_{r,i}$, $\Delta G_{a,i}$, $\Delta G_{int,i}$, $\Delta G_{r,BRI}$, $\Delta G_{a,BRI}$, $\Delta G_{int,BRI}$, C_{dl}, f_{BRI}, ρ_{CUS}, and j_{max}) are shown in detail in Table S4.

The analysis of the free reaction energies (ΔG^0) of the elementary steps of the OER mechanism on CUS at the surface of post-calcined Ir-oxide samples (Figure 9a) reveals that the fourth PCET step (*OOH ⇌ *OO + H^+ + e^-; step 6) consistently exhibited the highest free reaction energy among all samples, highlighting its crucial role as the potential determining step of the OER. The free reaction energy of this elementary step increases slightly with the increasing calcination temperature, following the same trend with the second and third PCET steps on CUS. These results indicate that the degree of crystallinity has a minor influence on the free reaction energy of the PCET processes. Similarly, the second water adsorption step (*O + H_2O ⇌ *OH_2O; step 4) emerges with the highest free reaction energy among the chemical steps in all samples, suggesting a chemical limitation on the OER performance. Notably, the free reaction energy of this step—and all other sorption processes—decreases slightly with increasing calcination temperature, indicating that they become thermodynamically more favorable with increasing crystallinity and decreasing hydroxide concentration at the surface. This trend may be attributed to reducing lateral repulsion among adsorbates, making sorption steps more favorable.[48,49] Also, diminishing the highly hydrated, defect-rich environment that stabilizes charge during proton-coupled electron transfer results in higher free reaction energies for

https://doi.org/10.1021/acscatal.5c03350
ACS Catal. XXXX, XXX, XXX−XXX

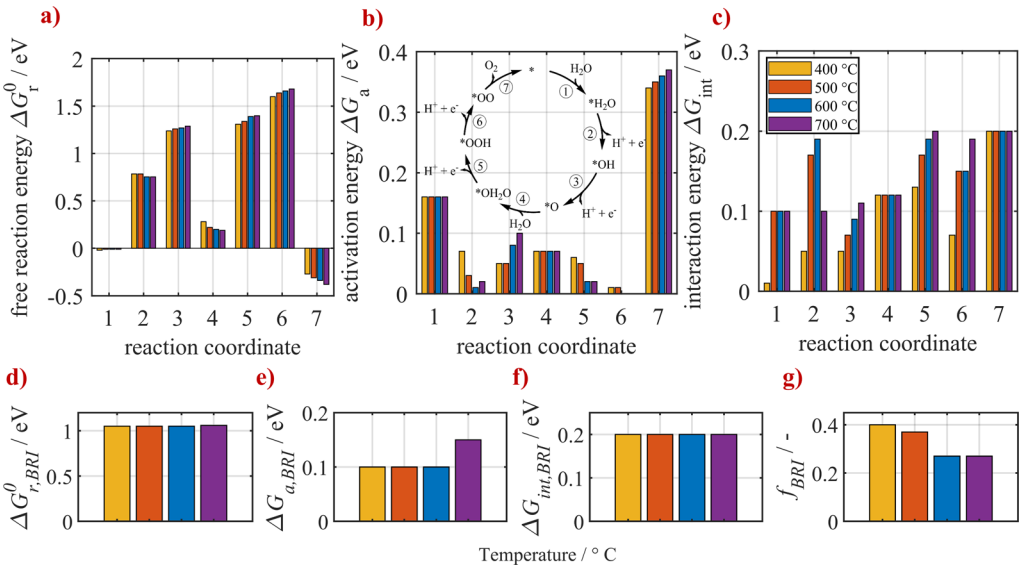

Figure 9. Energy diagrams for all the elementary steps (1−7) of the OER on the post-calcined Ir-oxide nanoparticles: (a) free reaction energies, (b) activation energies with the inset showing the OER mechanism with the numbers denoting the reaction steps,[10] and (c) interaction energies. Comparison of energies for the one-electron redox transition on BRI for the post-calcined Ir-oxide nanoparticles: (d) free reaction energies, (e) activation energies, and (f) interaction energies. Bar colors correspond to calcination temperatures and are consistent across the subfigures (a−g). The values are identified at the electrochemical standard conditions of a = 1 and T = 25 °C and at E = 0 V. The fraction of bridge sites for each IrO_x sample is reported in subfigure (g).

PCET steps on CUS.[6,50,51] Taken together, increasing crystallinity eases adsorption by reducing the adsorbate−adsorbate interaction and heterogeneity, but it slightly hinders PCET by reducing interfacial solvation and proton-shuttling, thereby increasing the required reaction energy for forming and stabilizing intermediates. Also, Figure 9d shows that the bridge-site redox on BRI remains thermodynamically in the same potential window as the second and third OER steps on CUS ($\Delta G_{r,BRI} \approx 1.15$ eV across all samples), which supports the notion that the 0.9−1.3 V region can reflect a superposition of the BRI redox process and early CUS PCET, as mentioned in Section 3.2. However, the bridge fraction f_{BRI} decreases with calcination (Figure 9g), and thus, despite similar $\Delta G_{r,BRI}$, the population of electrochemically available BRI (μ_2) sites shrinks. As a result, the intensity in the region between 0.9 and 1.3 V decreases with increasing crystallinity, and the apparent BRI−CUS overlap reduces, leaving the redox processes more strongly governed by CUS kinetics at higher calcination temperatures. Overall, higher crystallinity makes adsorption thermodynamically more favorable but raises the barriers for CUS-mediated PCET. Together with a larger CUS share and an overall drop in total site density (ρ), the net effect is a lower current response in the kinetically dominated potential (e.g., $j_{@1.53\ V,sim}$), explaining the concurrent decreases in ρ_{BRI} and $j_{@1.53\ V,sim}$ in Figure 8. The activation energies for all PCET steps on CUS remain consistently low across the samples, ranging from 0 to 0.1 eV (Figure 9b). These low values suggest minimal differences between the post-calcined samples and imply negligible kinetic barriers for the proton-coupled electron transfer processes on CUS. Similarly, the one-electron redox reaction on BRI shows a constant activation barrier (0.1 eV) across samples in Figure 9e, except for the IrO_x calcined at 700 °C with $\Delta G_{a,BRI}$ = 0.15 eV. In contrast to CUS-PCET and BRI redox process, the first water adsorption (* + H_2O ⇌ *H_2O; step 1 in Figure 9b) and the oxygen desorption (*OO → * + O_2; step 7) steps on CUS present activation energies above 0.1 eV for all post-calcined samples. Notably, oxygen desorption displays a significant activation barrier above 0.4 eV, becoming the kinetically limiting step during the OER despite its thermodynamic favorability. Moreover, the activation energy of this step increases with increasing calcination temperature, further indicating the influence of crystallinity on the OER kinetics.

Comparison of the lateral interaction energies extracted for each elementary step on CUS demonstrates two clear trends with an increasing calcination temperature, as shown in Figure 9c. First, the interaction energies associated with the PCET steps on CUS (*H_2O ⇌ *OH + H^+ + e^-: step 2, *OH ⇌ *O + H^+ + e^-: step 3, *OH_2O ⇌ *OOH + H^+ + e^-: step 5, and *OOH ⇌ *OO + H^+ + e^-: step 6) have mainly an increasing trend with increasing calcination temperature. Second, the interaction energies for the sorption steps (* + H_2O ⇌ *H_2O: step 1, *O + H_2O ⇌ *OH_2O: step 4, *OO → * + O_2: step 7) remain essentially constant across samples. For the bridge-site redox process (BRI−OH ⇌ BRI−O), the lateral interaction parameter also remains constant at 0.20 eV (Figure 9f). These results are physically consistent with the accompanying increase in crystallinity. Higher crystallinity yields a more ordered structure with fewer defects and weaker local solvation/proton-shuttling, so coverage-dependent penalties for charged PCET intermediates (*OH, *OOH) increase as captured by the larger $\Delta G_{int,i}$. In contrast, the water adsorption steps (OER steps 1 and 4) and the oxygen desorption step (OER step 7) are less sensitive to such adsorbate interactions. On the other hand, a constant $\Delta G_{int,BRI}$ indicates a local two-state interaction for μ_2−OH/μ_2−O that does not evolve with crystallinity. All in all, the analysis of the elementary steps of the OER on CUS and one-electron redox step on BRI reveals that increasing crystallinity predominantly hampers the PCET processes on CUS during the OER and raises the activation barrier for oxygen desorption. While the reduction in active site density remains the primary factor for the decline in the

https://doi.org/10.1021/acscatal.5c03350
ACS Catal. XXXX, XXX, XXX−XXX

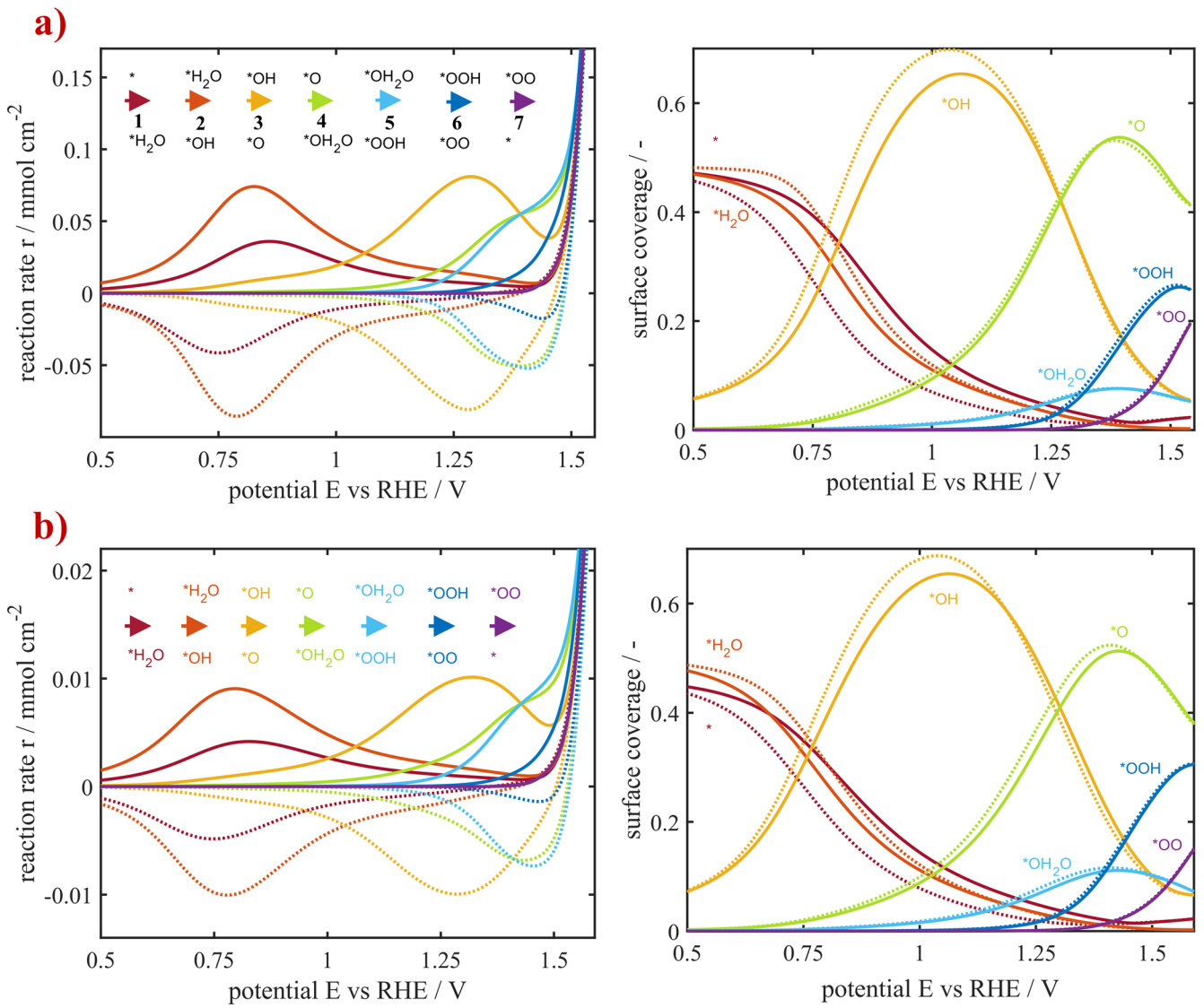

Figure 10. Effective reaction rates of the elementary steps of the OER mechanism on CUS (left-hand side) and surface coverage of the adsorbed species (right-hand side) obtained from the simulations of the cyclic voltammograms with the scan rate of 200 mV s^{-1} for Ir-oxide nanoparticles calcined at (a) 400 °C and (b) 700 °C. Forward and backward potential sweeps are indicated by the solid and dashed lines, respectively.

level of the OER performance, the changes in surface processes likely account for the observed non-linear relationship between active site density and catalytic activity.

In the following, we analyze how the changed surfaces and parameters impact the state of the surface species during cyclic voltammetry. Figure 10 shows the influence of the applied potential on the reaction rates of the individual steps of the OER on CUS and the surface coverage of the adsorbed species of the Ir-oxide samples calcined at 400 and 700 °C during the third cycle of their CV. As the reaction rates of the post-calcined samples are axisymmetric during the forward and backward scans, this indicates high reversibility of the reactions. The high similarity of the surface coverage of the adsorbed species during the forward and backward scans also supports this reversible behavior. Moreover, the results indicate that all the post-calcined iridium oxide nanoparticles are limited by the same elementary steps of the OER mechanism as can be seen from the species covering the surface at the potentials where the OER takes place. All of the other samples are given in Figure S14 for better visualization. In the following, we analyze the reaction rates and the surface coverage of the adsorbed species to deconvolute these limitations for each post-calcined Ir-oxide sample.

The analysis of post-calcined iridium oxide nanoparticles reveals that the CUS facilitated OER is limited at the potentials 1.5−1.6 V by the same surface processes, i.e., the second water adsorption (step 4), the fourth PCET (step 6), and the oxygen detachment (step 7). At these potentials, the *OO coverage decreases due to calcination at higher temperatures (19.5%, 17.2%, 16.4%, 15.0%, respectively, for 400, 500, 600, 700 °C), the *O coverage drops slightly (41.4%, 39.1%, 39.0%, 38.1%), and the *OOH coverage increases modestly (25.7%, 29.8%, 29.5%, 30.5%). Given the increase in the activation barrier for oxygen-desorption and the reaction free energy for the fourth PCET step of OER, the change in coverages indicates that higher crystallinity makes the *OOH ⇌ *OO + H^+ + e^- transition less favorable and O_2 release slower. As a result, the high-potential surface holds a somewhat larger fraction in *OOH and a smaller fraction in *OO at the same potential, which contributes to a lower current density in the 1.5−1.6 V

https://doi.org/10.1021/acscatal.5c03350
ACS Catal. XXXX, XXX, XXX−XXX

window. Consistent with this picture, Figure S15 shows that the bridge-site hydroxide coverage, θ_{BRI-OH}, begins near unity at ~0.8 V and decreases to 0 by ~1.3 V for all samples, meaning that the BRI redox process is mostly done by the onset of the OER. Notably, the 700 °C sample exhibits hysteresis for θ_{BRI-OH}, indicating a slower BRI redox transition at high crystallinity, consistent with its slightly larger activation barrier and stronger local interactions. Overall, increasing crystallinity shifts the high-potential balance toward *OOH via a larger free reaction energy and slows the detachment of the O_2 molecule via a larger activation barrier. At the same time, the BRI contribution in the 0.9−1.3 V range becomes more reversible for lower-temperature samples and shows more hysteresis for the most crystalline one. Overall, these trends indicate that increasing crystallinity redistributes surface populations toward *OOH and slows O_2 detachment while completing most of the BRI redox process below ~1.3 V. Combined with a reduced BRI fraction, f_{BRI}, and a lower total site density, ρ, the net effect is a diminished OER performance at 1.5−1.6 V. In other words, beyond the loss of available active sites due to calcination, intrinsic thermodynamic and kinetic changes increasingly govern the CV shape and activity. These findings underscore the importance of catalyst synthesis methods, emphasizing the subtle yet significant impact of crystallinity on the OER performance.

4. CONCLUSIONS

In this study, we investigated the impact of calcination temperature on the catalyst state, specifically the structure, morphology, and oxidation state of iridium oxide nanoparticles after their synthesis with flame spray pyrolysis and the resulting reaction kinetics and free energies during the oxygen evolution reaction (OER) in proton exchange membrane water electrolysis (PEMWE). To establish this link, we systematically integrated material characterization, electrochemical analysis, and dynamic microkinetic modeling to elucidate how variations in crystallinity and particle size translate into changes in active site density, double-layer capacitance, surface energies, and, ultimately, catalytic performance.

XRD measurements revealed the transformation of amorphous-like tetragonal rutile IrO_2 to crystalline phases with increased crystallinity and crystallite size at higher calcination temperatures. XPS measurements further confirmed structural transformations through shifts in binding energies for Ir−O by ~0.3 eV induced by calcination. Across all post-calcined samples, Ir(IV) remained the dominant oxidation state, with the possible presence of a Ir(III) fraction, and the Ir(IV)/Ir(III) ratio increased at higher temperatures. This trend coincided with a decrease in surface hydroxide species from ~42% in the as-prepared sample to ~24% at 700 °C, potentially hindering water adsorption. TEM imaging provided insights into the morphology of iridium oxide nanoparticles, showing a significant increase in the mean particle size from 4 to 30 nm when the calcination temperature increased from 400 to 700 °C. These morphological changes were correlated with variations in electrochemical performance, emphasizing the importance of morphology control in catalyst design. CV measurements further demonstrated a decline in double-layer capacitance and active site density with increasing calcination temperature, leading to a reduction in OER activity. This effect aligns well with the decrease in iridium hydroxide surface species of the catalysts in XPS as well as the changes in the estimated apparent capacitances from ~4.02 $\mu F\ cm^{-2}$ (400 °C) to ~0.35 $\mu F\ cm^{-2}$ (700 °C). Moreover, shifts in onset potentials and peak intensities indicated possible changes in reaction, activation, and interaction energies induced by calcination temperature. Dynamic microkinetic modeling, including an independent one-electron redox transition on bridge-sites in addition to the seven-step OER mechanism on CUS sites, reproduced the experimental voltammograms and provided quantitative insights into changes in the reaction rates, surface coverages, and free energies. The analysis revealed that the PCET steps exhibited slightly higher free reaction energies while retaining low activation barriers (≤0.1 eV), whereas the sorption processes became thermodynamically more favorable with increasing calcination temperature. In contrast, activation barriers for the oxygen desorption (step 7) increase with increasing calcination temperature, thus limiting the OER. The BRI redox process is independent of that on CUS sites and contributes to the CV between 0.9 and 1.3 V. Its surface fraction, f_{BRI} decreases with calcination temperature. Consequently, at higher potentials, the current density becomes majorly governed by CUS kinetics. Taken together with the sharp decrease in the total density of active sites, these changes reduce the OER performance despite improved water adsorption, showing that the degree of crystallinity also influences the reaction free energies and activation energies of PCET. Overall, our work shows that the main reason for the loss of the OER performance with increasing calcination temperature is the reduction in active site density caused by particle growth as well as changes in the Ir(IV)/Ir(III) surface oxidation state. Beyond this extrinsic site loss, higher crystallinity subtly changes intrinsic energies: it slightly raises the reaction free energies of the PCET steps on CUS, increases the activation barrier for O_2 desorption, and lowers both the fractional contribution and reversibility of the bridge-site redox (decreasing f_{BRI}), while adsorption thermodynamics become marginally more favorable.

These findings highlight the complex interplay among catalyst structure, morphology, oxidation state, and electrochemical performance in PEMWE. By elucidating the underlying mechanisms governing the OER, our study provides in-depth information for the development of advanced catalyst design strategies to improve energy conversion efficiency and enhance sustainable technologies for green hydrogen production. While our methods are demonstrated for the OER, the principles and insights gained into the structure−performance relationship are also applicable to other electrocatalytic processes, offering potential pathways for optimizing catalysts across various reactions in renewable energy technologies.

■ ASSOCIATED CONTENT

Data Availability Statement

Source data are provided with this paper in the KITopen repository under DOI: 10.35097/vf3j9gx4te0ftpqc.

Supporting Information

The Supporting Information is available free of charge at https://pubs.acs.org/doi/10.1021/acscatal.5c03350.

Experimental details on XRD, TEM, SEM, and XPS analyses and additional results; electrochemical measurements and electrocatalytic results; bulk resistances obtained from EIS measurements; additional details on the microkinetic model; and simulation results obtained from the microkinetic model (PDF)

https://doi.org/10.1021/acscatal.5c03350
ACS Catal. XXXX, XXX, XXX−XXX

AUTHOR INFORMATION

Corresponding Authors

Philipp Röse − *Institute for Applied Materials−Electrochemical Technologies, Karlsruhe Institute of Technology, 76131 Karlsruhe, Germany;* orcid.org/0000-0001-6591-7133; Email: philipp.roese@kit.edu

Ulrike Krewer − *Institute for Applied Materials−Electrochemical Technologies, Karlsruhe Institute of Technology, 76131 Karlsruhe, Germany;* orcid.org/0000-0002-5984-5935; Email: ulrike.krewer@kit.edu

Authors

Gözde Kardeş − *Institute for Applied Materials−Electrochemical Technologies, Karlsruhe Institute of Technology, 76131 Karlsruhe, Germany;* orcid.org/0000-0002-4213-7983

Leonie Wildersinn − *Institute for Applied Materials−Energy Storage Systems, Karlsruhe Institute of Technology, D-76344 Karlsruhe, Germany*

Fabian Jeschull − *Institute for Applied Materials−Energy Storage Systems, Karlsruhe Institute of Technology, D-76344 Karlsruhe, Germany;* orcid.org/0000-0002-5927-1978

Svetlana Korneychuk − *Institute for Applied Materials−Materials Science and Engineering, Karlsruhe Institute of Technology, 76131 Karlsruhe, Germany; Karlsruhe Nano Micro Facility (KNMFi), Karlsruhe Institute of Technology, 76344 Eggenstein-Leopoldshafen, Germany; Institute of Nanotechnology, Karlsruhe Institute of Technology, 76344 Eggenstein-Leopoldshafen, Germany*

Astrid Pundt − *Institute for Applied Materials−Materials Science and Engineering, Karlsruhe Institute of Technology, 76131 Karlsruhe, Germany*

Jan-Dierk Grunwaldt − *Institute for Chemical Technology and Polymer Chemistry, Karlsruhe Institute of Technology, 76131 Karlsruhe, Germany;* orcid.org/0000-0003-3606-0956

Complete contact information is available at: https://pubs.acs.org/10.1021/acscatal.5c03350

Author Contributions

G.K. calcined the as-prepared Ir-oxide samples, designed and performed RDE and XRD measurements, conducted parameterization and simulation work, and analyzed the results. L.W. performed the XPS measurements, including evaluation and analysis of the data. S.K. performed the HAADF-STEM measurements, including analysis of the data. J.D.G. provided as-prepared Ir-oxide samples. F.J., A.P., and J.D.G. provided valuable comments on the interpretation of the results and reviewed the manuscript. P.R. and U.K. supervised the work, contributed to data analysis and interpretation, and were responsible for the funding acquisition. G.K. wrote the original draft. All authors reviewed and edited the manuscript and have given approval to the final version of the manuscript.

Notes

The authors declare no competing financial interest.

ACKNOWLEDGMENTS

We gratefully acknowledge the funding from the Federal Ministry of Education and Research, Germany (BMBF, Project StacIE: 03HY103C) and the German Research Foundation (DFG, SPP 2080: KR 3850/8-1, GR 3987/15-1). We thank Steffen Czioska for synthesizing the pristine Ir-oxide sample, Celine Kopp for supporting with the RDE measurements on the post-calcined samples, and Annette Schucker for taking the SEM pictures. We further acknowledge the support of the Karlsruhe Nano Micro Facility (KNMFi, www.knmf.kit.edu), a Helmholtz Research Infrastructure at Karlsruhe Institute of Technology with the sTEM measurements. We also acknowledge the use of ChatGPT (https://chat.openai.com/) while writing this manuscript to improve the academic tone and accuracy of language, including grammatical structures, punctuation, and vocabulary.

REFERENCES

(1) Lv, X.-W.; Tian, W.-W.; Yuan, Z.-Y. Recent Advances in High-Efficiency Electrocatalytic Water Splitting Systems. *Electrochem. Energy Rev.* **2023**, *6* (1), 23.

(2) Raveendran, A.; Chandran, M.; Dhanusuraman, R. A Comprehensive Review on the Electrochemical Parameters and Recent Material Development of Electrochemical Water Splitting Electrocatalysts. *RSC Adv.* **2023**, *13* (6), 3843−3876.

(3) Rossmeisl, J.; Qu, Z.-W.; Zhu, H.; Kroes, G.-J.; Nørskov, J. K. Electrolysis of Water on Oxide Surfaces. *J. Electroanal. Chem.* **2007**, *607* (1−2), 83−89.

(4) Cherevko, S.; Reier, T.; Zeradjanin, A. R.; Pawolek, Z.; Strasser, P.; Mayrhofer, K. J. J. Stability of Nanostructured Iridium Oxide Electrocatalysts during Oxygen Evolution Reaction in Acidic Environment. *Electrochem. Commun.* **2014**, *48*, 81−85.

(5) Kasian, O.; Geiger, S.; Li, T.; Grote, J.-P.; Schweinar, K.; Zhang, S.; Scheu, C.; Raabe, D.; Cherevko, S.; Gault, B.; Mayrhofer, K. J. J. Degradation of Iridium Oxides via Oxygen Evolution from the Lattice: Correlating Atomic Scale Structure with Reaction Mechanisms. *Energy Environ. Sci.* **2019**, *12* (12), 3548−3555.

(6) Geiger, S.; Kasian, O.; Shrestha, B. R.; Mingers, A. M.; Mayrhofer, K. J. J.; Cherevko, S. Activity and Stability of Electrochemically and Thermally Treated Iridium for the Oxygen Evolution Reaction. *J. Electrochem. Soc.* **2016**, *163* (11), 3132−3138.

(7) Danilovic, N.; Subbaraman, R.; Chang, K.-C.; Chang, S. H.; Kang, Y. J.; Snyder, J.; Paulikas, A. P.; Strmcnik, D.; Kim, Y.-T.; Myers, D.; Stamenkovic, V. R.; Markovic, N. M. Activity-Stability Trends for the Oxygen Evolution Reaction on Monometallic Oxides in Acidic Environments. *J. Phys. Chem. Lett.* **2014**, *5* (14), 2474−2478.

(8) Mom, R. V.; Falling, L. J.; Kasian, O.; Algara-Siller, G.; Teschner, D.; Crabtree, R. H.; Knop-Gericke, A.; Mayrhofer, K. J. J.; Velasco-Vélez, J.-J.; Jones, T. E. Operando Structure−Activity−Stability Relationship of Iridium Oxides during the Oxygen Evolution Reaction. *ACS Catal.* **2022**, *12* (9), 5174−5184.

(9) Cherevko, S.; Geiger, S.; Kasian, O.; Kulyk, N.; Grote, J.-P.; Savan, A.; Shrestha, B. R.; Merzlikin, S.; Breitbach, B.; Ludwig, A.; Mayrhofer, K. J. J. Oxygen and Hydrogen Evolution Reactions on Ru, RuO 2, Ir, and IrO 2 Thin Film Electrodes in Acidic and Alkaline Electrolytes: A Comparative Study on Activity and Stability. *Catal. Today* **2016**, *262*, 170−180.

(10) Geppert, J.; Röse, P.; Czioska, S.; Escalera-López, D.; Boubnov, A.; Saraçi, E.; Cherevko, S.; Grunwaldt, J.-D.; Krewer, U. Microkinetic Analysis of the Oxygen Evolution Performance at Different Stages of Iridium Oxide Degradation. *J. Am. Chem. Soc.* **2022**, *144* (29), 13205−13217.

(11) Escalera-López, D.; Czioska, S.; Geppert, J.; Boubnov, A.; Röse, P.; Saraçi, E.; Krewer, U.; Grunwaldt, J.-D.; Cherevko, S. Phase- and Surface Composition-Dependent Electrochemical Stability of Ir-Ru Nanoparticles during Oxygen Evolution Reaction. *ACS Catal.* **2021**, *11* (15), 9300−9316.

(12) Pfeifer, V.; Jones, T. E.; Velasco Vélez, J. J.; Massué, C.; Greiner, M. T.; Arrigo, R.; Teschner, D.; Girgsdies, F.; Scherzer, M.; Allan, J.; Hashagen, M.; Weinberg, G.; Piccinin, S.; Hävecker, M.; Knop-Gericke, A.; Schlögl, R. The Electronic Structure of Iridium Oxide Electrodes Active in Water Splitting. *Phys. Chem. Chem. Phys.* **2016**, *18* (4), 2292−2296.

(13) Karimi, F.; Bazylak, A.; Peppley, B. A. Effect of Calcination Temperature on the Morphological and Electrochemical Characteristics of Supported Iridium Hydroxyoxide Electrocatalysts for the PEM Electrolyzer Anode. *J. Electrochem. Soc.* **2017**, *164* (4), 464−474.
(14) Abbott, D. F.; Lebedev, D.; Waltar, K.; Povia, M.; Nachtegaal, M.; Fabbri, E.; Copéret, C.; Schmidt, T. J. Iridium Oxide for the Oxygen Evolution Reaction: Correlation between Particle Size, Morphology, and the Surface Hydroxo Layer from Operando XAS. *Chem. Mater.* **2016**, *28* (18), 6591−6604.
(15) Czioska, S.; Boubnov, A.; Escalera-López, D.; Geppert, J.; Zagalskaya, A.; Röse, P.; Saraçi, E.; Alexandrov, V.; Krewer, U.; Cherevko, S.; Grunwaldt, J.-D. Increased Ir−Ir Interaction in Iridium Oxide during the Oxygen Evolution Reaction at High Potentials Probed by Operando Spectroscopy. *ACS Catal.* **2021**, *11* (15), 10043−10057.
(16) Kim, Y.-T.; Lopes, P. P.; Park, S.-A.; Lee, A.-Y.; Lim, J.; Lee, H.; Back, S.; Jung, Y.; Danilovic, N.; Stamenkovic, V.; Erlebacher, J.; Snyder, J.; Markovic, N. M. Balancing Activity, Stability and Conductivity of Nanoporous Core-Shell Iridium/Iridium Oxide Oxygen Evolution Catalysts. *Nat. Commun.* **2017**, *8* (1), 1449.
(17) Kim, M. G.; Kang, J. M.; Lee, J. E.; Kim, K. S.; Kim, K. H.; Cho, M.; Lee, S. G. Effects of Calcination Temperature on the Phase Composition, Photocatalytic Degradation, and Virucidal Activities of TiO2 Nanoparticles. *ACS Omega* **2021**, *6* (16), 10668−10678.
(18) Xu, J.; Wang, M.; Liu, G.; Li, J.; Wang, X. The Physical−Chemical Properties and Electrocatalytic Performance of Iridium Oxide in Oxygen Evolution. *Electrochim. Acta* **2011**, *56* (27), 10223−10230.
(19) Reier, T.; Teschner, D.; Lunkenbein, T.; Bergmann, A.; Selve, S.; Kraehnert, R.; Schlögl, R.; Strasser, P. Electrocatalytic Oxygen Evolution on Iridium Oxide: Uncovering Catalyst-Substrate Interactions and Active Iridium Oxide Species. *J. Electrochem. Soc.* **2014**, *161* (9), 876−882.
(20) Elmaalouf, M.; Odziomek, M.; Duran, S.; Gayrard, M.; Bahri, M.; Tard, C.; Zitolo, A.; Lassalle-Kaiser, B.; Piquemal, J.-Y.; Ersen, O.; Boissière, C.; Sanchez, C.; Giraud, M.; Faustini, M.; Peron, J. The Origin of the High Electrochemical Activity of Pseudo-Amorphous Iridium Oxides. *Nat. Commun.* **2021**, *12* (1), 3935.
(21) Usama, M.; Razzaq, S.; Hattig, C.; Steinmann, S. N.; Exner, K. S. Oxygen Evolution Reaction on IrO2(110) Is Governed by Walden-Type Mechanisms. *Nat. Commun.* **2025**, *16* (1), 6137.
(22) Liang, C.; Rao, R. R.; Svane, K. L.; Hadden, J. H. L.; Moss, B.; Scott, S. B.; Sachs, M.; Murawski, J.; Frandsen, A. M.; Riley, D. J.; Ryan, M. P.; Rossmeisl, J.; Durrant, J. R.; Stephens, I. E. L. Unravelling the Effects of Active Site Density and Energetics on the Water Oxidation Activity of Iridium Oxides. *Nat. Catal.* **2024**, *7* (7), 763−775.
(23) Ping, Y.; Nielsen, R. J.; Goddard, W. A. The Reaction Mechanism with Free Energy Barriers at Constant Potentials for the Oxygen Evolution Reaction at the IrO(2) (110) Surface. *J. Am. Chem. Soc.* **2017**, *139* (1), 149−155.
(24) Over, H. Fundamental Studies of Planar Single-Crystalline Oxide Model Electrodes (RuO 2, IrO 2) for Acidic Water Splitting. *ACS Catal.* **2021**, *11* (14), 8848−8871.
(25) Geppert, J.; Kubannek, F.; Röse, P.; Krewer, U. Identifying the Oxygen Evolution Mechanism by Microkinetic Modelling of Cyclic Voltammograms. *Electrochim. Acta* **2021**, *380*, 137902.
(26) Nong, H. N.; Falling, L. J.; Bergmann, A.; Klingenhof, M.; Tran, H. P.; Spöri, C.; Mom, R.; Timoshenko, J.; Zichittella, G.; Knop-Gericke, A.; Piccinin, S.; Pérez-Ramírez, J.; Cuenya, B. R.; Schlögl, R.; Strasser, P.; Teschner, D.; Jones, T. E. Key Role of Chemistry versus Bias in Electrocatalytic Oxygen Evolution. *Nature* **2020**, *587* (7834), 408−413.
(27) Liang, C.; Rao, R.; Svane, K.; Hadden, J.; Moss, B.; Scott, S.; Sachs, M.; Murawski, J.; Frandsen, A.; Riley, J.; Ryan, M.; Durrant, J.; Rossmeisl, J.; Stephens, I. Unravelling the Effects of Active Site Densities and Energetics on the Water Oxidation Activity of Iridium Oxides. In *Proceedings of the Materials for Sustainable Development Conference (MAT-SUS)*; FUNDACIO DE LA COMUNITAT VALENCIANA SCITO, 2023.
(28) Motagamwala, A. H.; Dumesic, J. A. Microkinetic Modeling: A Tool for Rational Catalyst Design. *Chem. Rev.* **2021**, *121* (2), 1049−1076.
(29) Chen, D.; Shang, C.; Liu, Z.-P. Machine-Learning Atomic Simulation for Heterogeneous Catalysis. *npj Comput. Mater.* **2023**, *9* (1), 2.
(30) Geppert, J.; Röse, P.; Pauer, S.; Krewer, U. Microkinetic Barriers of the Oxygen Evolution on the Oxides of Iridium, Ruthenium and Their Binary Mixtures. *ChemElectroChem* **2022**, *9* (20), No. e202200481.
(31) Noh, H.; Mayer, J. M. Medium-Independent Hydrogen Atom Binding Isotherms of Nickel Oxide Electrodes. *Chem* **2022**, *8* (12), 3324−3345.
(32) Schmickler, W.; Santos, E. *Interfacial Electrochemistry*; Springer Berlin Heidelberg: Berlin, Heidelberg, 2010.
(33) Hwang, B. H. Shifts of Peak Positions Due to Specimen Geometry and Beam Divergence in X-Ray Diffractometer. *Powder Diffr.* **1996**, *11* (4), 276−280.
(34) Kwon, S.; Stoerzinger, K. A.; Rao, R.; Qiao, L.; Goddard, W. A.; Shao-Horn, Y. Facet-Dependent Oxygen Evolution Reaction Activity of IrO $_2$ from Quantum Mechanics and Experiments. *J. Am. Chem. Soc.* **2024**, *146* (17), 11719−11725.
(35) Pfeifer, V.; Jones, T. E.; Velasco Vélez, J. J.; Massué, C.; Arrigo, R.; Teschner, D.; Girgsdies, F.; Scherzer, M.; Greiner, M. T.; Allan, J.; Hashagen, M.; Weinberg, G.; Piccinin, S.; Hävecker, M.; Knop-Gericke, A.; Schlögl, R. The Electronic Structure of Iridium and Its Oxides. *Surf. Interface Anal.* **2016**, *48* (5), 261−273.
(36) Stoerzinger, K. A.; Qiao, L.; Biegalski, M. D.; Shao-Horn, Y. Orientation-Dependent Oxygen Evolution Activities of Rutile IrO2 and RuO2. *J. Phys. Chem. Lett.* **2014**, *5* (10), 1636−1641.
(37) Bozack, M. J. Sputter-Induced Modifications of IrO2 During XPS Measurements. *Surf. Sci. Spectra* **1993**, *2* (2), 123−127.
(38) Smith, R. D. L.; Sporinova, B.; Fagan, R. D.; Trudel, S.; Berlinguette, C. P. Facile Photochemical Preparation of Amorphous Iridium Oxide Films for Water Oxidation Catalysis. *Chem. Mater.* **2014**, *26* (4), 1654−1659.
(39) Siracusano, S.; Baglio, V.; Grigoriev, S. A.; Merlo, L.; Fateev, V. N.; Aricò, A. S. The Influence of Iridium Chemical Oxidation State on the Performance and Durability of Oxygen Evolution Catalysts in PEM Electrolysis. *J. Power Sources* **2017**, *366*, 105−114.
(40) Roiron, C.; Wang, C.; Zenyuk, I. V.; Atanassov, P. Oxygen 1s X-Ray Photoelectron Spectra of Iridium Oxides as a Descriptor of the Amorphous−Rutile Character of the Surface. *J. Phys. Chem. Lett.* **2024**, *15* (45), 11217−11223.
(41) Batchelor-McAuley, C. Defining the Onset Potential. *Curr. Opin. Electrochem.* **2023**, *37*, 101176.
(42) Zagalskaya, A.; Evazzade, I.; Alexandrov, V. Ab Initio Thermodynamics and Kinetics of the Lattice Oxygen Evolution Reaction in Iridium Oxides. *ACS Energy Lett.* **2021**, *6* (3), 1124−1133.
(43) Exner, K. S.; Over, H. Beyond the Rate-Determining Step in the Oxygen Evolution Reaction over a Single-Crystalline IrO 2 (110) Model Electrode: Kinetic Scaling Relations. *ACS Catal.* **2019**, *9* (8), 6755−6765.
(44) Conway, B. E.; Mozota, J. Surface and Bulk Processes at Oxidized Iridium Electrodes—II. Conductivity-Switched Behaviour of Thick Oxide Films. *Electrochim. Acta* **1983**, *28* (1), 9−16.
(45) Saveleva, V. A.; Wang, L.; Teschner, D.; Jones, T.; Gago, A. S.; Friedrich, K. A.; Zafeiratos, S.; Schlögl, R.; Savinova, E. R. Operando Evidence for a Universal Oxygen Evolution Mechanism on Thermal and Electrochemical Iridium Oxides. *J. Phys. Chem. Lett.* **2018**, *9* (11), 3154−3160.
(46) Binninger, T.; Mohamed, R.; Waltar, K.; Fabbri, E.; Levecque, P.; Kötz, R.; Schmidt, T. J. Thermodynamic Explanation of the Universal Correlation between Oxygen Evolution Activity and Corrosion of Oxide Catalysts. *Sci. Rep.* **2015**, *5* (1), 12167.

https://doi.org/10.1021/acscatal.5c03350
ACS Catal. XXXX, XXX, XXX−XXX

(47) Binninger, T.; Kowalski, P. M.; Eikerling, M. H. Oxygen Desorption − Critical Step for the Oxygen Evolution Reaction. *Curr. Opin. Electrochem.* **2023**, *42*, 101382.
(48) Bard, A. J.; Faulkner, L. R.; White, H. S. *Electrochemical Methods*; John Wiley \& Sons: 2022.
(49) Koper, M. T. M. Thermodynamic Theory of Multi-Electron Transfer Reactions: Implications for Electrocatalysis. *J. Electroanal. Chem.* **2011**, *660* (2), 254−260.
(50) Hammes-Schiffer, S.; Stuchebrukhov, A. A. Theory of Coupled Electron and Proton Transfer Reactions. *Chem. Rev.* **2010**, *110* (12), 6939−6960.
(51) Warren, J. J.; Tronic, T. A.; Mayer, J. M. Thermochemistry of Proton-Coupled Electron Transfer Reagents and Its Implications. *Chem. Rev.* **2010**, *110* (12), 6961−7001.

https://doi.org/10.1021/acscatal.5c03350
ACS Catal. XXXX, XXX, XXX−XXX